Important Notice

UNIVERSITY OF CALGARY

Analysis and application of the Radon transform

by

Zhihong Cao

A THESIS

SUBMITTED TO THE FACULTY OF GRADUATE STUDIES

IN PARTIAL FULFILMENT OF THE REQUIREMENTS FOR THE

DEGREE OF MASTER OF SCIENCE

DEPARTMENT OF GEOLOGY AND GEOPHYSICS

CALGARY, ALBERTA

December, 2006

UNIVERSITY OF CALGARY

FACULTY OF GRADUATE STUDIES

The undersigned certify that they have read, and recommend to the Faculty of Graduate Studies for acceptance, a thesis entitled "Analysis and application of the Radon transform" submitted by Zhihong Cao in partial fulfilment of the requirements of the degree of Master of Science.

Supervisor, Dr. John C. Bancroft, Department of Geology and Geophysics

---

Dr. Larry R. Lines, Department of Geology and Geophysics

Dr. Len Bos, Department of Mathematics and Statistics

Date

Abstract

An ultimate goal of seismic exploration is to generate accurate images of the subsurface to clearly identify hydrocarbon plays. Seismic data processing plays an important role in achieving this goal. One of the key problems in seismic data processing is to attenuate multiple reflections from seismic data. Multiple reflections often destructively interfere with primary reflections and lead to incorrect seismic images.

Different approaches have been investigated and applied to the multiple attenuation problem, including the Radon transform which is an industry standard and has been attracting a lot of attention in the last two decades. In this thesis, Radon transform techniques are reviewed and analyzed and a new Radon algorithm, the optimized semblance-weighted Radon transform, is introduced. An overview of various Radon transform methods is given and the algorithms tested on synthetic and real data.

Acknowledgements

Without the support I received from everybody in the department, I would not have enjoyed my study and work here at the University of Calgary. This thesis became a possibility through many contributions from many people. The CREWES Project and sponsors, the Department of Geology and Geophysics, the Society of Exploration Geophysicists, and the Canadian Society of Exploration Geophysicists all financially supported my research and education.

First of all, I would like to thank Dr. John C. Bancroft, my supervisor, for his guidance and support, and James Brown, who guided me in my first year of study at the University of Calgary. All the CREWES staff and students have provided meaningful discussions, suggestions and warm friendship. Special thanks go to Hanxing Lu, David Henley, Arnim Hasse, Chuck Ursenbach, Kevin Hall and Rolf Maier for their geophysical and computer systems expertise. Louise Forgues successfully managed the administrative work. It has been a pleasure to work with Chunyan Xiao, Xiang Du, Carlos Montana and Carlos Nieto.

Special and great thanks go to Mark Ng in Geo-X System Ltd. He developed the theory of the optimized-weighted Radon transform and spent time discussing the theory with me. It was a great pleasure for me to know and study this algorithm and to finally successfully apply it to the datasets.

I can never give enough thanks to my parents, sister, and brother for their great encouragement and trust in me during difficult times. Without my husband's spiritual support, it would have been much more difficult for me to have concentrated on my research.

Dedication

To my parents

Table of Contents

List of Figures and Illustrations

Symbols and Abbreviations

Symbol	Definition
CDP	Common Depth Point
CMP	Common Mid-Point
CSP	Common Scatter Point
DRT	Discrete Radon transform
NMO	Normal Moveout
RMS	Root Mean Square
d	Data space
f-k	Frequency-wavenumber
p	Ray parameter
q	Horizontal Radon parameter
x	Offset
t	Two-way traveltime
t_0	Two-way zero-offset traveltime
u	Radon space
τ	The intercept traveltime
ω	Angular frequency

Chapter One: Introduction

Seismic exploration is widely used in the petroleum industry for hydrocarbon discovery. The ultimate goal of seismic exploration is to image and interpret subsurface structures—the results of which depend on seismic data processed with tried and tested techniques. Seismic data processing is one of the major steps in the exploration process, alongside the acquisition and interpretation of seismic data.

1.1 Basic concepts of seismology

This section is devoted to basic concepts used in exploration seismology, especially those used in this thesis.

Seismic data are acquired in the field by many pairs of sources and receivers. Signals generated by a source located on the surface propagate into the earth and will be reflected back to the surface after it hits a subsurface interface. Receivers on the surface will record the reflected signals. A few basic concepts are reviewed as follows.

Common mid-point (CMP) gather

A common mid-point (CMP) gather is defined as the data collection of traces that share the same mid-point position. A midpoint is the middle point between a source and receiver pair. An example of the geometry of a CMP gather is shown in Figure 1.1. For the three pairs of source points and receivers, they have the same midpoint M on the surface. The point D is the midpoint on the reflector and is also called the mid-depth point, which is also shared by the three pairs of sources and receivers.

The variable offset, the distance between each source and receiver pair, is one of the two dimensions of CMP gathers. The other dimension is time, which is the traveltime

that the signal spends on the travel path from its source point to reflector and then to receiver.

The common depth point (CDP) gather is the same as a CMP gather for a single horizontal interface. But they are not the same for dipping interfaces. A CMP gather is one of the most frequently used concepts in this thesis.

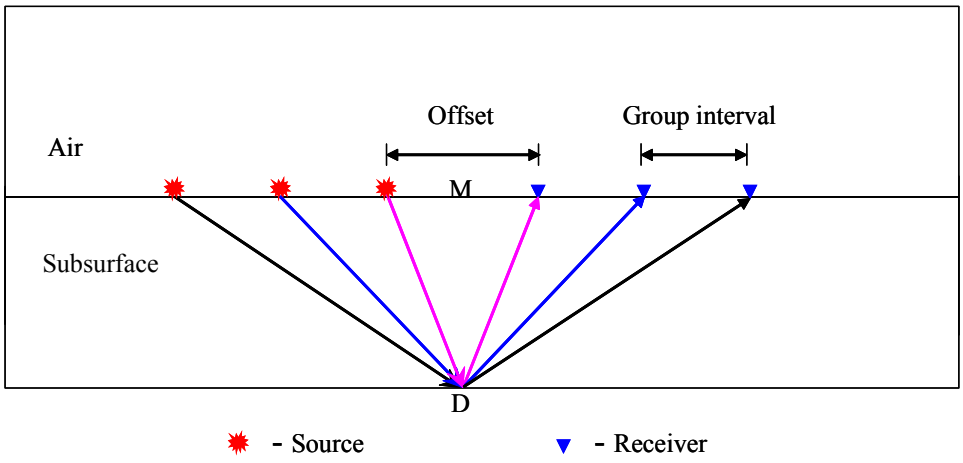

Figure 1.1 Geometry of a common mid-point (CMP) gather.

Normal moveout (NMO) correction

If the model in Figure 1.1 is a constant velocity model, the traveltime $t(x)$ of a CMP gather along the raypath from a source to D then back to the associated surface receiver is defined as (Figure 1.2):

$$t^2(x) = t_0^2 + x^2/v^2 \ , \qquad (1.1.1)$$

where x is offset, the distance between the source and the associated receiver, v is the velocity of the medium above the reflector, and t_0 is the two-way vertical traveltime along MD or the two-way zero offset traveltime. For a flat reflector as introduced in Figure 1.1, Equation (1.1.1) describes a hyperbola with its apex at the zero offset trace in

the two-way time-versus-offset plane (Yilmaz, 1987). A CMP gather illustrated in Figure 1.3 shows the hyperbolic event associated with the model in Figure 1.1 and Equation (1.1.1). The difference between the two-way traveltime $t(x)$ at offset x and the zero-offset time t_0 is called the normal moveout or NMO (Figure 1.3), which can be defined by the following equation:

$$\Delta t_{NMO} = t(x) - t_0 . \tag{1.1.2}$$

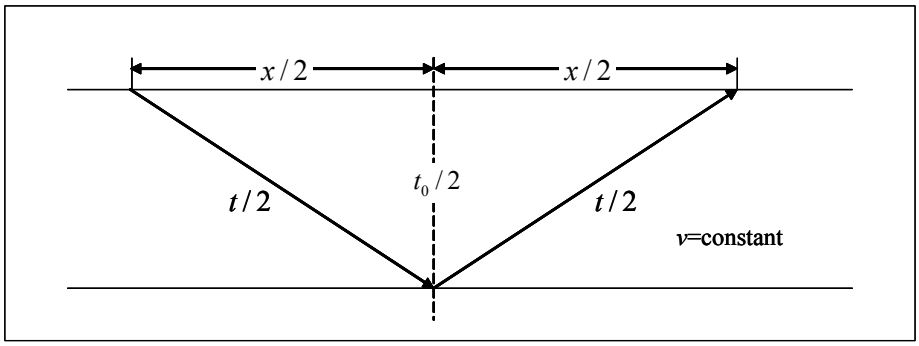

Figure 1.2 The sketch of the traveltime associated with Figure 1.1.

The process of NMO correction aims to remove the moveout effect on traveltime along the offset dimension. The ideal result of NMO correction of Figure 1.3 is shown in Figure 1.4. However, in practice, the wavelet will be distorted and stretched after NMO correction.

Normal moveout is a very basic and important seismology concept. The Radon transform, which is the main topic of this thesis and will be discussed later, has a very strong relationship with this concept.

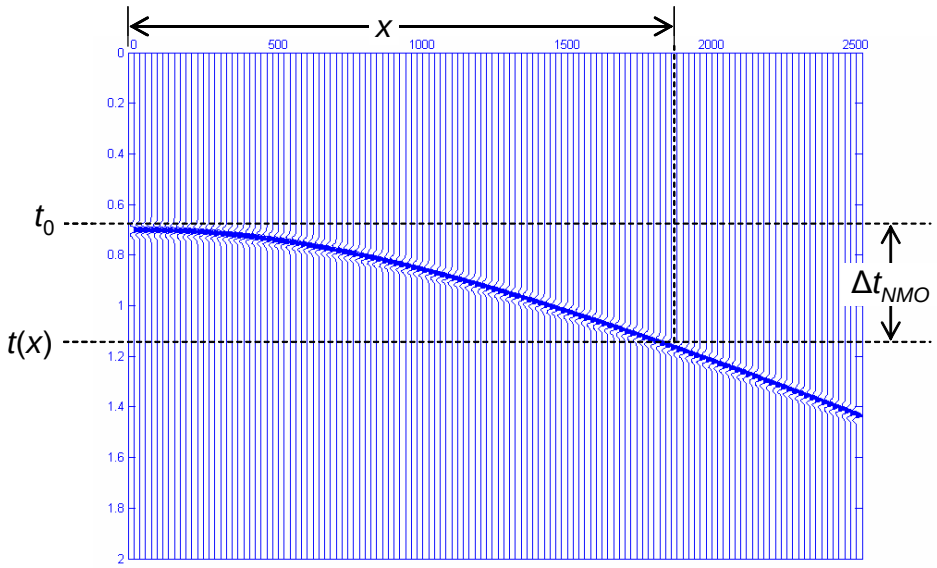

Figure 1.3 A single-side CMP gather associated with the geometry in Figure 1.1.

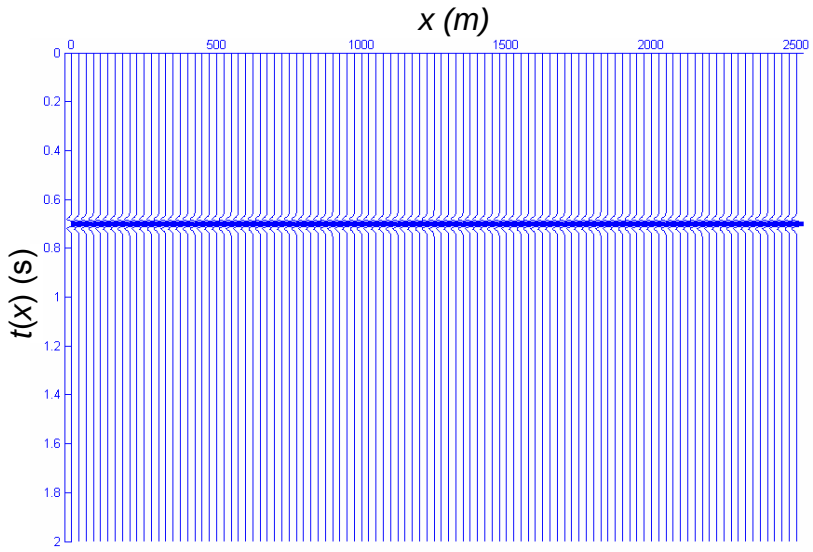

Figure 1.4 The ideal result of NMO correction in Figure 1.3.

CMP stack

The CMP stacking technique is proposed by Mayne (1962). It is a process of gathering the data from NMO-corrected CMP gathers and summing them over offsets. The primary associated signals are enhanced by integration over offsets while random noise attenuated since primaries are flat on NMO-corrected gathers. Therefore, the signal-to-noise ratio is improved after the CMP stacking technique is applied.

Root Mean Square (RMS) velocity

In the case of a horizontal layered earth model as shown in Figure 1.5, the NMO velocity in Equation (1.1.1) is replaced by the Root Mean Square (RMS) velocity:

$$t^2(x) = t_0^2 + x^2 / v_{rms}^2 \,, \tag{1.1.3}$$

where the RMS velocity v_{rms} is defined by the Dix equation (Dix, 1955) as given by:

$$v_{rms} = \sqrt{\sum_{k=1}^{N} \Delta\tau_k v_k^2 \Big/ \sum_{k=1}^{N} \Delta\tau_k} \,, \tag{1.1.4}$$

where v_k is the interval velocity of the k^{th} layer in the model, $\Delta\tau_k$ is the vertical traveltime in the k^{th} layer and N is the total number of layers above t_0.

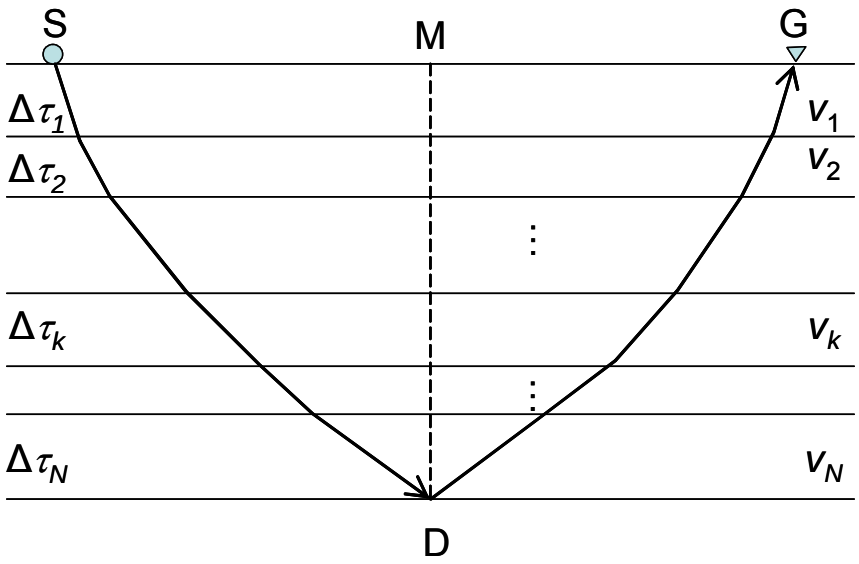

Figure 1.5 A horizontal layered earth model.

1.2 Historical background to multiple reflections

Seismic data are acquired by using energy sources to generate elastic waves which are reflected back to receivers on the surface by subsurface structures. An example of a simple seismic data acquisition geometry, with one source and a pair of receivers is shown in Figure 1.6. Primary reflections are those reflected only once at a certain subsurface interface before they arrive at the receivers. These primary reflections provide us with useful information such as velocities and subsurface structural identification. Seismic imaging techniques are developed based on primary reflections.

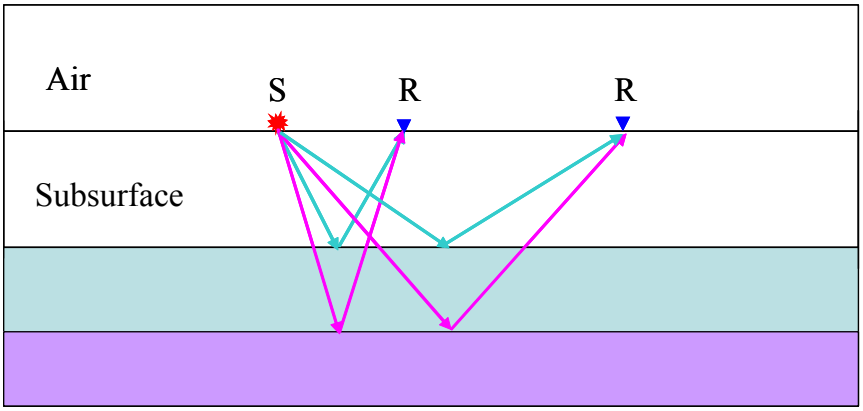

Figure 1.6 Seismic data acquisition geometry and primary reflections.

However, in addition to primary reflections, receivers also pick up multiple reflections, which have been reflected between subsurface reflectors or the surface more than once before being received on the surface. Multiple reflections often destructively interfere with primary reflections and lead to poor seismic images. The removing of multiples from reflection seismograms has been a longstanding problem in exploration geophysics. Multiple reflections yield dramatic effects especially on marine seismic surveys. Because of the extremely high impedance contrast between the water surface and the air, the reflection coefficient of the water-air surface is close to -1. If the water bottom is solid, the water layer can trap energy between the water surface and water bottom. In this case, multiple reflections can be much stronger than primary reflections. Energy trap-related multiples include water-column reverberations (Figure 1.7) and peg-leg multiples (Figure 1.8). Another major type of multiple is an interbed multiple, shown in Figure 1.9, which can happen, for example, in environments with salt.

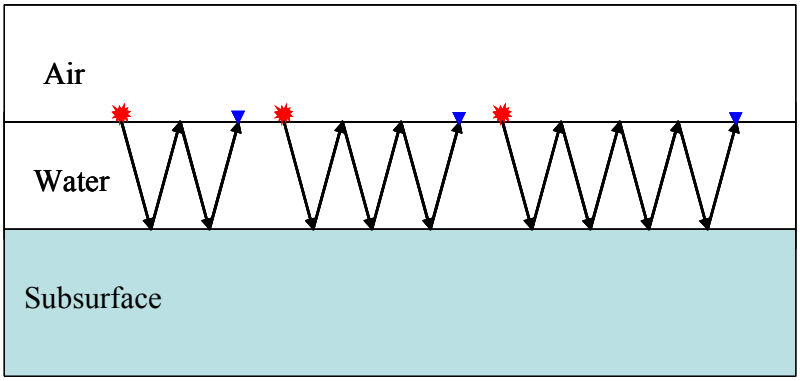

Figure 1.7 Water-column reverberations.

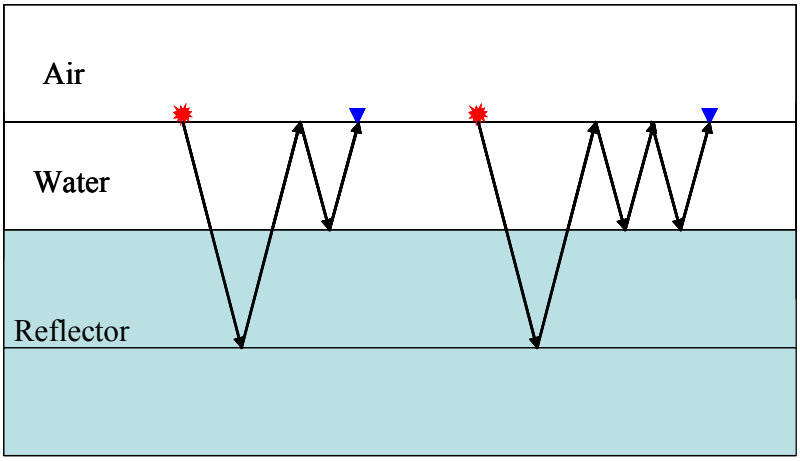

Figure 1.8 Peg-leg multiples.

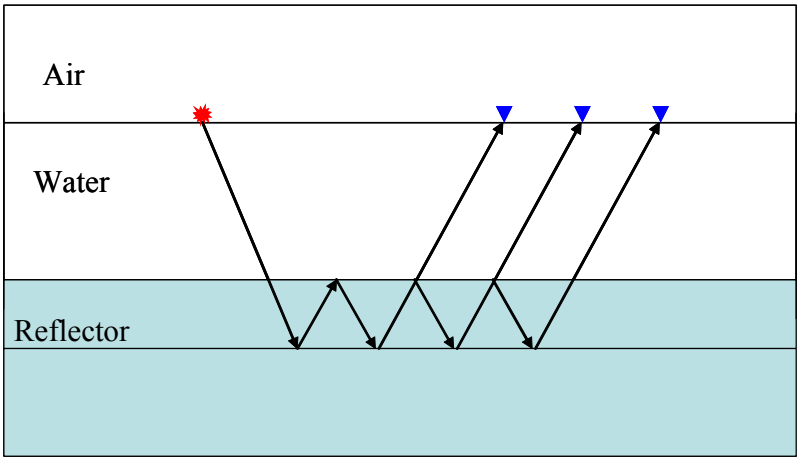

Figure 1.9 Interbed multiples.

1.3 Review of typical solutions to multiple attenuation

Before the seismic exploration industry employed the common midpoint (CMP) or common depth point (CDP) stacking techniques, multiple identification was used to help interpret and recognize primaries (Ellsworth, 1948). The main characteristics of multiple reflections include: (1) traveltime; (2) normal moveout; (3) periodicity of events; and (4) moveout of dipping reflectors. Backus (1959) may have been the first person to attempt to attenuate water reverberations using an inverse filter—the basis of predictive deconvolution—using the reverberations' periodic characteristic. The theory of predictive deconvolution itself was proposed by Peacock and Treitel (1969).

The fact that multiples and primaries exhibit different moveout traveltimes is the theoretical underpinning of many other multiple-attenuation techniques, such as the CMP stacking technique, the *f-k* filter and the Radon transform. Mayne (1962) proposed multiple suppression using CMP or CDP stacking techniques based on velocity differences between primaries and multiples. Typically a primary has less moveout than a multiple. If NMO correction is applied using the primary velocities, then the primaries on the collected CMP gathers tend to be flat and aligned with each other while the multiples are undercorrected and attenuated when they are stacked (Mayne, 1962 and Yilmaz, 2001). This is considered to be the most robust and effective way to suppress multiples and random noise (Foster and Mosher, 1992).

The dipping information of events is preserved when they are mapped into the *f-k* domain using the 2-D Fourier transform. If a CMP gather is moveout-corrected using a velocity mid-way between the primary and the multiple velocities, the primary reflection will be over-corrected and the multiple reflection under-corrected, meaning that they will

appear in different quadrants in the *f-k* domain and thereby most of the energies are separated from each other (Yilmaz, 1987 and 2001).

The Karhunen-Loeve (K-L) transform, which optimally extracts coherent multiple information from multichannel input data, uses the moveout difference between multiples and primaries to attenuate multiples in seismic data processing when CMP gathers are corrected using the multiple velocities (Hemon and Mace, 1978; Jones, 1985; Jones and Levy, 1987).

1.4 The Radon transform

The Radon transform is a mathematical technique that has been widely used in seismic data processing and image analysis. Three types of Radon transforms have been used as multiple-attenuation techniques in seismic data processing: the slant-stack or τ-p transform; the hyperbolic Radon transform; and the parabolic Radon transform (Trad, 2001). The slant-stack transform can be combined with predictive deconvolution to attenuate multiples in the prestack seismic data based on the periodic characteristic of multiples, which is discussed in Chapter 2. In contrast to the slant-stack transform, the hyperbolic and parabolic Radon transforms are applied to multiple attenuation based on moveout discrimination between multiples and primaries. In this thesis, I will focus more on analyzing these two types of the Radon transform.

The Radon transform was first established by Johan Radon (1917). Deans (1983) discusses the mathematical theory, and Durrani and Bisset (1984) examine the fundamental properties of the Radon transform. Thorson and Claerbout (1985) utilized the hyperbolic Radon transform as a velocity analysis tool, and the parabolic Radon transform was applied for the first time as a multiple attenuation technique by Hampson

(1986). Since then, Radon transforms have become one of the most widely used approaches in attenuating multiples (for example Bradshaw and Ng, 1987; Kelamis *et al*., 1990; Kostov, 1990; Foster and Mosher, 1992; Hugonnet and Canadas, 1995; Sacchi and Ulrych, 1995; Cary, 1998; Sacchi and Porsani, 1999; Trad, 2001; Oppert, 2002; Trad *et al*., 2002 and 2003; Ng and Perz, 2004).

However, the resolution of Radon transforms has always been a serious problem for geophysicists: investigators have been trying to enhance the focusing power of the transform for decades.

1.5 Objective of the thesis

This thesis reviews various methods associated with multiple attenuation in seismic exploration, with most attention being applied to Radon transforms. Different approaches to Radon transforms are analyzed. The scope of this thesis is to evaluate the advantages and disadvantages of the various Radon algorithms.

Because time domain methods are computationally expensive, Radon transforms are often implemented in the frequency domain. A high-resolution, or optimized, semblance-weighted Radon transform, which is comparable to the frequency domain methods in computational expense, is discussed with regard to the time-space domain. Synthetic datasets are used to test different Radon algorithms and the optimized semblance-weighted Radon approach is also applied to a real dataset from the White Rose area off the east coast of Canada.

1.6 My contributions in this thesis

- Different approaches to multiple attenuation in seismology are reviewed;

- Various Radon transform approaches are discussed and evaluated with synthetic datasets;
- The optimized semblance-weighted Radon transform is coded;
- The optimized semblance-weighted Radon transform is applied to the real seismic dataset.

1.7 Outline of thesis

The structure of this thesis is as follows:

- Chapter 1 provides the background for my research;
- Chapter 2 reviews different methods associated with multiple attenuation;
- Chapter 3 reviews and analyzes the various types and algorithms of the Radon transform;
- Chapter 4 evaluates the Radon algorithms with both synthetic and real data.
- Chapter 5 summarizes my research and provides a discussion of the most relevant findings.

Chapter Two: Review of multiple suppression techniques

This chapter provides an overview of the multiple attenuation techniques which have been used in the oil and gas exploration industry.

2.1 CMP stack technique

The CMP stacking technique is the most robust and effective way to suppress multiples in seismology (Foster and Mosher, 1992). Due to the different velocities between primaries and multiples, a primary has different, typically less, moveout than a multiple reflection on a CMP gather. If NMO correction is applied to CMP gathers using the primary velocities, the primaries are flattened while multiples are under-corrected (Yilmaz, 2001). When the CMP stacking technique is performed on these NMO-corrected CMP gathers, the primaries are enhanced because of the superposition of events at the zero offset traveltime, while the multiples are spread over a range of time to produce smaller amplitudes.

2.2 Predictive deconvolution

Predictive deconvolution is a proven multiple suppression method based on the periodicity of multiple reflections (Yilmaz, 1987).

Theory

The desired output as a time-advanced form of the input series for deconvolution produces a predictive process. For a given input series $x(t)$ at a future time $t+\alpha$, its value $x(t+\alpha)$ can be predicted by a prediction filter, where α is called the prediction lag. The prediction filter can be estimated by solving the following matrix equation (Peacock and Treitel, 1969):

$$\begin{bmatrix} r_0 & r_1 & r_2 & \mathrm{L} & r_{n-1} \\ r_1 & r_0 & r_1 & \mathrm{L} & r_{n-2} \\ r_2 & r_1 & r_0 & \mathrm{L} & r_{n-3} \\ . & . & . & \mathrm{L} & . \\ . & . & . & \mathrm{L} & . \\ . & . & . & \mathrm{L} & . \\ r_{n-1} & r_{n-2} & r_{n-3} & \mathrm{L} & r_0 \end{bmatrix} \begin{bmatrix} a_0 \\ a_1 \\ a_2 \\ . \\ . \\ . \\ a_{n-1} \end{bmatrix} = \begin{bmatrix} r_\alpha \\ r_{\alpha+1} \\ r_{\alpha+2} \\ . \\ . \\ . \\ r_{\alpha+n-1} \end{bmatrix}, \tag{2.2.1}$$

where r_i is the i^{th} lag of the autocorrelation of the input trace $x(t)$, and a_i is the desired prediction filter coefficient, α is the prediction lag, and n is the operator length. Convolving this operator with the input trace and delaying it by the prediction lag results in the output at time $(t+\alpha)$, which can be written as the following equation:

$$y(t+\alpha) = x(t) * a(t), \tag{2.2.2}$$

where $*$ donates convolution, and $y(t+\alpha)$ is the output of the input trace at time $(t+\alpha)$.

For a horizontally layered system with a constant velocity, normal incidence has constant interval between multiples, such as water reverberations. In seismology, multiples are predictable components with a periodic rate of occurrence, while primaries are not. The prediction lag α is defined by the interval between the primary reflection of the water bottom and its first order multiple, which depends on the depth of the water layer. Multiples can be estimated by a prediction filter. Subtracting multiples from the input seismic data tends to produce multiple-free data. This flow is shown in Figure 2.1.

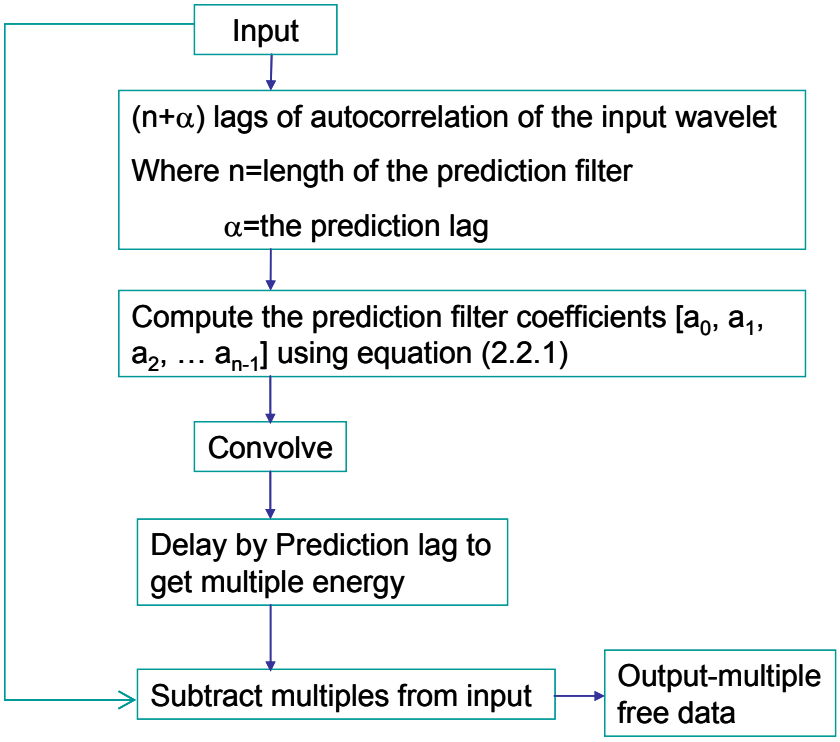

Figure 2.1 Predictive deconvolution using the prediction filter (after Yilmaz, 1989).

A prediction error filter can be designed by modifying the prediction filter:

$$\{1, \underbrace{0, 0, \mathrm{L}}_{(\alpha-1)\ \text{zeros}}, -a_0, -a_1, \mathrm{L}, -a_{n-1}\}, \tag{2.2.3}$$

The application of this filter essentially combines prediction, delay and subtracting as outlined in Figure 2.1. Multiple-free seismic data are output by convolving the input trace with the prediction error filter. A flowchart of this process is shown in Figure 2.2.

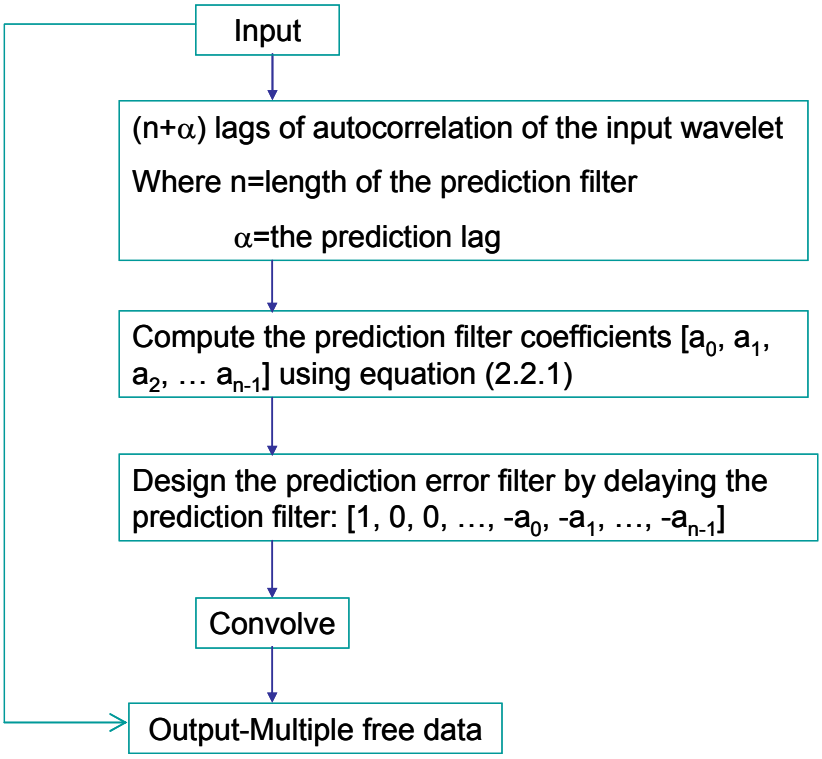

Figure 2.2 Predictive deconvolution using the prediction error filter (after Yilmaz, 1989).

Predictive deconvolution in the τ-p domain

The problem of predictive deconvolution in the x-t domain is that even for horizontally layered media, multiples are not periodic for non-zero offset traces. Alam and Austin (1981) proved that in the slant-stack or τ-p domain, the periodic characteristic of multiples is preserved for non-zero offset traces. A primary, a first order multiple, and a second order multiple with the same offset x in Figure 2.3 are used to explain why multiples are not periodic in the x-t domain. The traveltimes of the primary, the first order multiple and the second order multiple are represented by t_p, t_{m1} and t_{m2}, respectively.

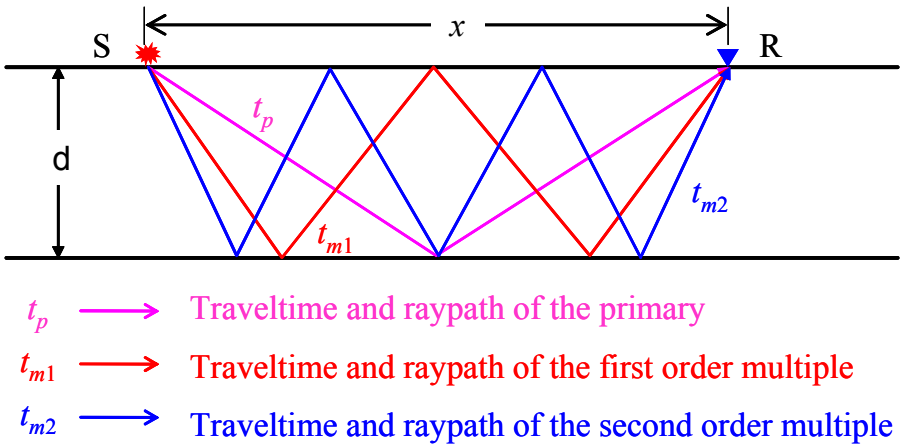

Figure 2.3 Multiples with the same offset are not periodic in time.

According to Equation (1.1.1), we can get expressions for each of the traveltimes as follows:

$$t_p = \sqrt{t_0^2 + (x/v)^2}\,, \tag{2.2.4}$$

$$t_{m1} = 2\sqrt{t_0^2 + (x/2v)^2}\,, \tag{2.2.5}$$

$$t_{m2} = 3\sqrt{t_0^2 + (x/3v)^2}\,. \tag{2.2.6}$$

We can then easily get Δt_1, the interval between the first order multiple and the primary, and Δt_2, the interval between the second and the first order multiples as follows:

$$\Delta t_1 = 2\sqrt{t_0^2 + (x/2v)^2} - \sqrt{t_0^2 + (x/v)^2}\,, \tag{2.2.7}$$

$$\Delta t_2 = 3\sqrt{t_0^2 + (x/3v)^2} - 2\sqrt{t_0^2 + (x/2v)^2}\,. \tag{2.2.8}$$

It is not hard to observe that $\Delta t_1 \neq \Delta t_2$ at a non-zero offset x, which indicates that multiple reflections not periodic at a certain non-zero offset in the x-t domain.

The traveltimes of the primary and multiple events in this model are plotted in Figure 2.4, from which we can also visualize the non-periodic feature of multiples.

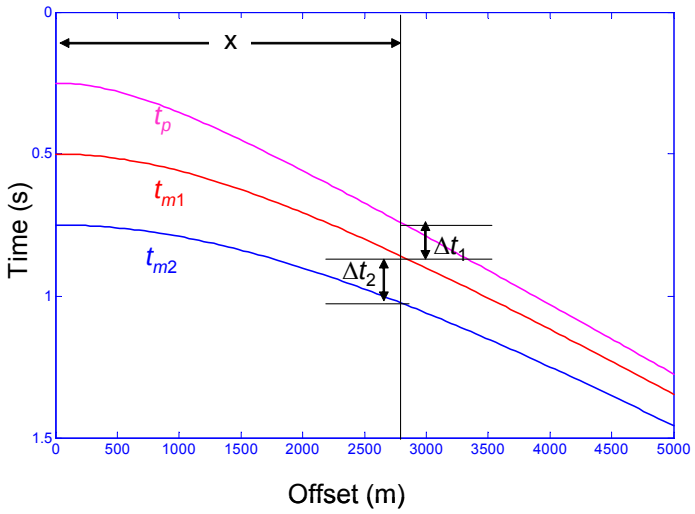

Figure 2.4 Sketch of a CMP gather illustrating traveltimes of the events in Figure 2.3.

The slant-stack transform

The slant-stack transform is one kind of Radon transform. Other terminologies for the transform are the linear Radon transform or the τ-p transform. It is defined by summing data in the time-offset domain along a linear path as:

$$S(\tau, p) = \sum_x d(t = \tau + px, x). \tag{2.2.9}$$

Here $S(\tau, p)$ represents a plane wave; $d(t, x)$ is a shot, CMP (common midpoint) or CSP (common scatter point, Bancroft *et al*., 1998) gather; τ is the two-way intercept traveltime; t is the two-way traveltime; x is offset; p is a ray parameter defined by $p = \sin\theta / v$ with wave travel velocity v and the incidence angle θ.

Theoretically, an event with linear moveout in the time-offset domain can be mapped to a point with the slant-stack transform, and a hyperbolic event, such as a primary or a multiple event, can be mapped to an ellipse in the τ-p domain as shown Figure 2.5 (Treitel *et al*, 1982).

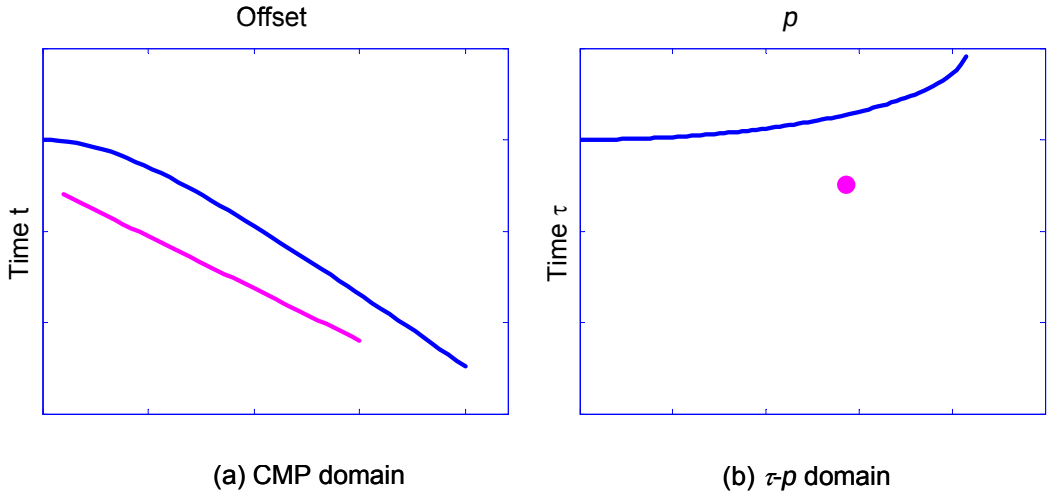

Figure 2.5 The linear and hyperbolic events in the CMP gather (a) and its slant-stack transform (b).

Application to multiple suppression

One of the features of the slant-stack transform is that multiples are periodic in time for all p traces in the τ-p domain (Taner, 1980; Alam and Austin, 1981; and Treitel *et al*., 1982). Predictive deconvolution can be applied in the τ-p domain to suppress multiples.

In the τ-p space, the traveltime equation is defined by an elliptic equation (Schultz and Claerbout, 1978):

$$\tau^2 = \tau_0^2 \left(1 - p^2 v^2\right). \tag{2.2.10}$$

Here τ_0 is the two-way vertical traveltime. The intercept traveltime for an n-bounce multiple in the τ-p space is described by:

$$\tau_n^2 = \left(n\tau_0\right)^2 \left(1 - p^2 v^2\right). \tag{2.2.11}$$

From Equations (2.2.10) and (2.2.11), it is easy to get $\tau_n = n\tau$, which means that multiple events in the τ-p space are exactly periodic in time. An example in the CMP domain as shown in Figure 2.6 (a), with the primary P and multiples M_1 and M_2, is

mapped into the τ-p space, as shown in Figure 2.6 (b). The intervals between P and M_1 and between M_1 and M_2 at a proposed trace p_0 in the τ-p space are the same.

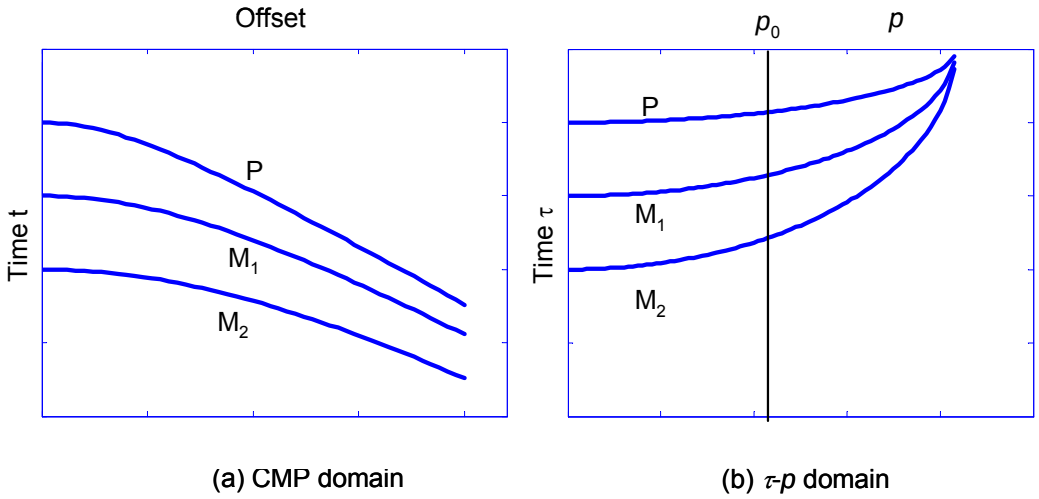

Figure 2.6 A CMP gather with a primary and its two multiple events and its τ-p stack.

2.3 Frequency-wavenumber (*f*-*k*) filter

Events with different slopes also show different slopes when they are mapped into the *f*-*k* domain. Therefore, if a CMP gather (Figure 2.7), which consists of primary and multiple events, is NMO-corrected with velocities between the primary velocities and multiple velocities (Figure 2.8), primaries will be over-corrected and multiples under-corrected. The left side of Figure 2.8 is the semblance plot, which contains velocity verse time information, of the model in Figure 2.7. Every focused point in the semblance plot provides velocity information for every hyperbolic event in the model. The multiple events have lower velocities compared to the primary events. The right side of Figure 2.8 shows the NMO-corrected CMP gather using the velocities between the primary velocities and multiple velocities. This NMO corrected CMP gather with primaries and multiples are mapped into different quadrants in the *f*-*k* space of Figure 2.9. An *f*-*k* filter

is also defined by the polygon in Figure 2.9. Energy inside the polygon represents primaries and passes the filter, while energy outside the polygon represents multiples and aliasing of both primaries and multiples and is muted. Inverse *f-k* transforming the filtered data produces an NMO-corrected multiple-free CMP gather (Figure 2.10 (a)). Inverse NMO-correction using the velocities which were used for the forward NMO-correction restores the multiple free primaries (Figure 2.10 (b)).

The disadvantage of the *f-k* filter is that the near-offset energy of primaries and multiples are mixed in the *f-k* domain because the near-offset data of both are horizontal. They can't be separated from each other in the *f-k* domain. That is why we still see residual energy of the multiples at near offsets in Figure 2.10.

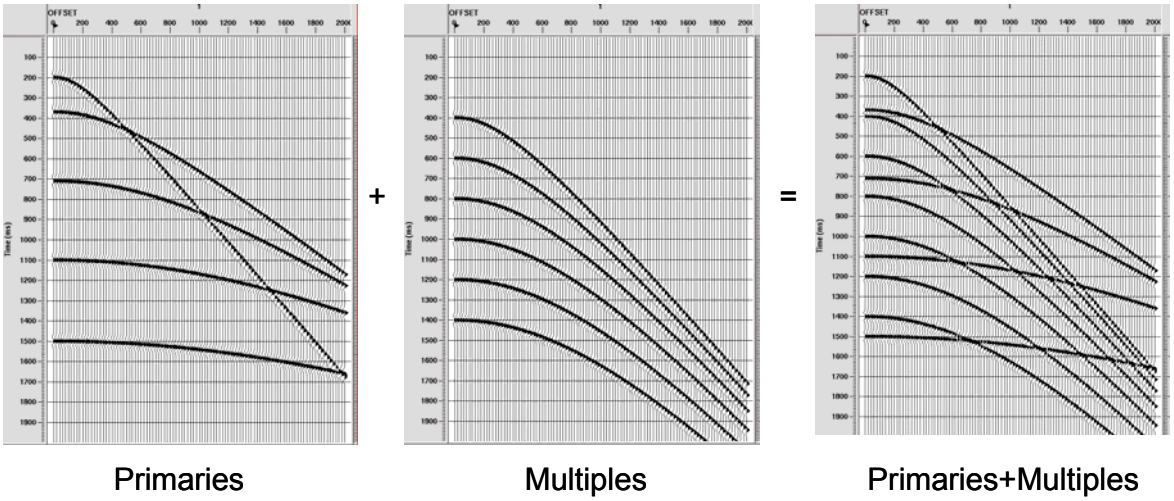

Figure 2.7 A synthetic CMP gather including primaries and multiples.

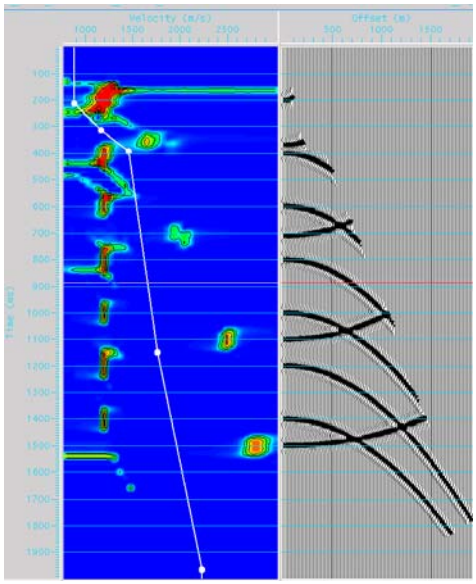

Figure 2.8 Velocities mid-way between the multiples and primaries for the model in Figure 2.7. Left: the semblance plot of the model provides velocity verse time information; Right: the NMO-corrected CMP gather using the velocities picked in the semblance plot.

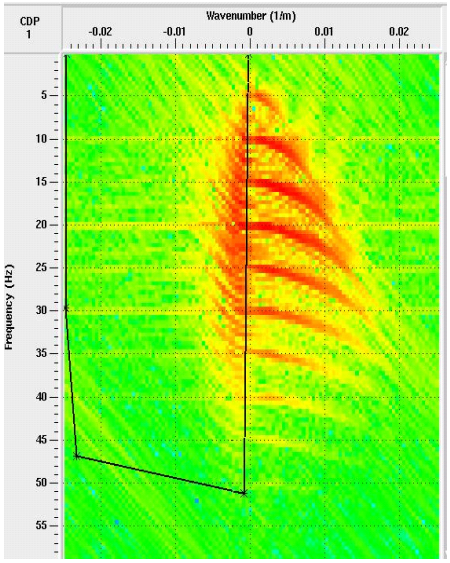

Figure 2.9 The *f-k* spectrum of the model in Figure 2.7. The polygon zone is primary energy.

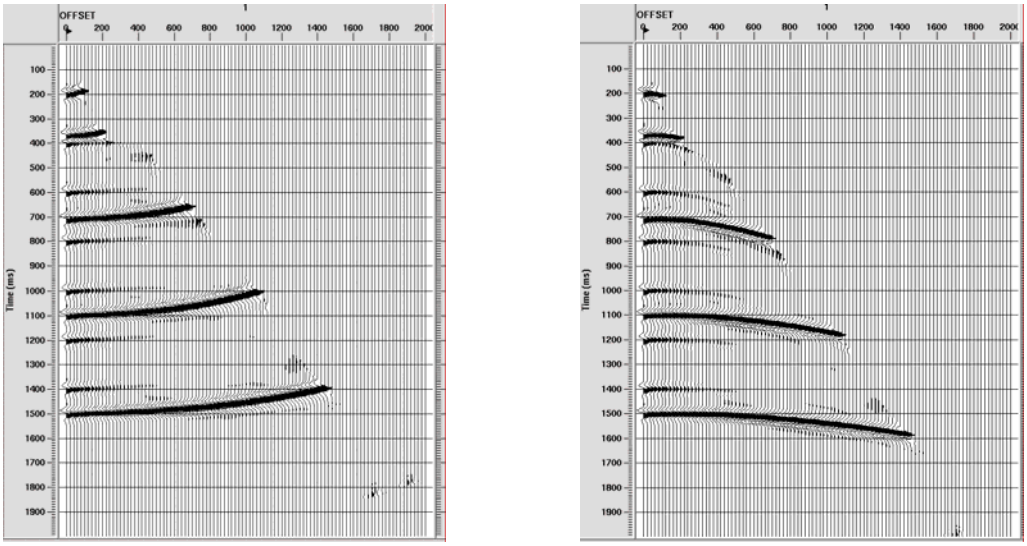

(a) (b)

Figure 2.10 (a) The NMO-corrected multiple free dataset after *f-k* filtering; (b) after inverse NMO-correction using the same velocity function as in Figure 2.8.

2.4 Karhunen-Loeve transform

The Karhunen-Loeve (K-L) transform, which optimally extracts coherent information from multichannel input data, uses the moveout difference between multiples and primaries to attenuate multiples in seismic data processing (Hemon and Mace, 1978; Jones, 1985; Jones and Levy, 1987). The basic concept of the K-L transform is that a two-dimensional dataset, such as a NMO-corrected CMP gather in the time-space domain, can be decomposed into a number of components (i.e., the eigenimages), starting with the first eigenimage that contains the highest correlatable events, in sequence, all the way down to the last eigenimage that comprises the least correlatable components (Yilmaz, 2001). If NMO-correction is applied to a CMP gather (Figure 2.11) using the velocity associated with the multiples, the multiples will be flattened and the primaries over-corrected or under-corrected, as shown in Figure 2.12 (a). These multiples will then be

the most coherent events in the gather and they will map into the first eigenimage of the K-L transform. By omitting the first few eigenimages (since the waveform of the multiples could be severely distorted by interfering primary events or by the NMO-correction) and reconstructing the NMO-corrected CMP gather from the rest of eigenimages in the K-L domain, one can obtain a CMP gather free of multiples associated with the velocity which was used for the NMO-correction (Figure 2.12 (b)).

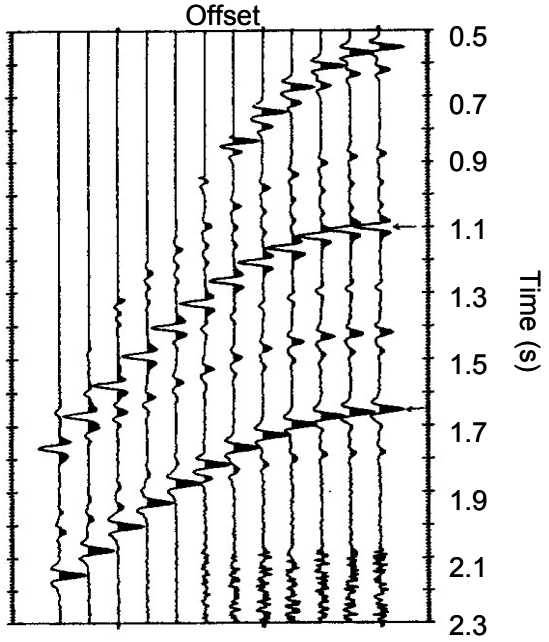

Figure 2.11 A synthetic CMP gather with multiple events at 1.10 s and 1.65 s which have a velocity of 1450 m/s (after Jones and Levy, 1987).

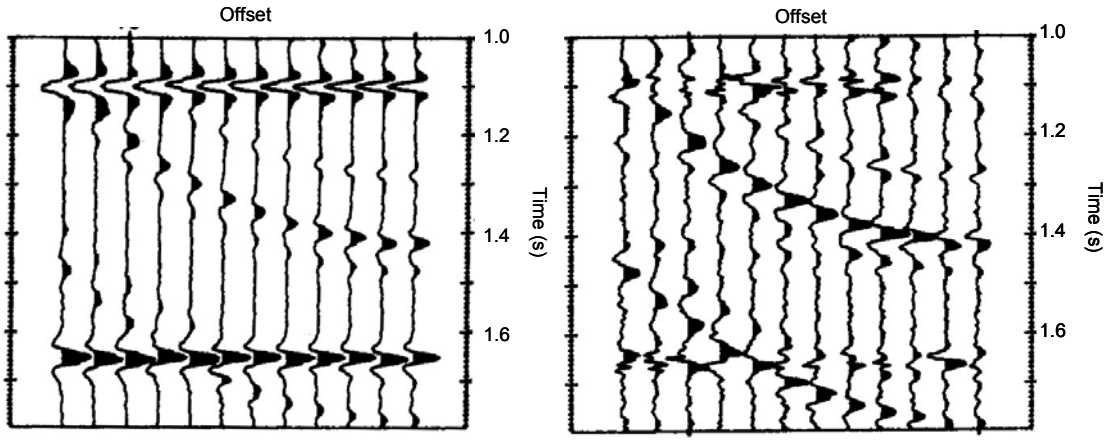

(a) (b)

Figure 2.12 (a) A data window after NMO-correction with a velocity of 1450 m/s; (b) Reconstructed data window omitting the first two eigenimages.

2.5 Radon transform

Johan Radon (1917) is credited with establishing the Radon transform, a function that integrates some physical property of a medium along a particular path. In seismology, the generalized Radon transform is defined as an integral of amplitudes:

$$u(\tau,q)=\int_{-\infty}^{\infty} d\left(t=\tau+q\varphi(x),x\right)dx\,, \tag{2.5.1}$$

where $d(x,t)$ is the original seismogram; $u(\tau,q)$ is its Radon transform; x is a spatial variable, such as offset; $\varphi(x)$ defines the curvature upon which the transform curve is defined; q is the slope of the curvature; τ is the intercept time; and t is the two-way traveltime. The discrete generalized Radon transform has the form:

$$u(\tau,q)=\sum_{x} d\left(t=\tau+q\varphi(x),x\right). \tag{2.5.2}$$

A few variations of the Radon transform have been explored in seismology including the slant-stack transform, which we discussed previously in Section 2.2, the parabolic Radon transform, the hyperbolic Radon transform, and the shifted-hyperbolic Radon transform.

As we mentioned in Section 2.2, ideally the slant-stack transform maps a linear event in the x-t domain to a focused point, and a hyperbolic event to an ellipse in the transformed domain (Figure 2.5), which can be explained by Equation (2.2.10). Multiples are periodic in the τ-p domain and predictive deconvolution can be applied in the τ-p domain to remove multiples.

The other variations of Radon transform, such as the parabolic, hyperbolic and shifted-hyperbolic Radon transform, ideally map events with corresponding patterns to focused points in the Radon domain. For example, the hyperbolic Radon transform is defined as integration by stacking the data along a hyperbolic path. An event with hyperbolic moveout in the time-space domain is mapped to a focused point in the model domain by the hyperbolic Radon transform. Both primaries and multiples are hyperbolic in the time-space domain of CMP gathers but with different velocities, as indicated by Equations (2.2.4) to (2.2.6), and they are mapped to different regions in the Radon domain when the hyperbolic Radon transform is applied. The parabolic Radon transform can be applied to an NMO-corrected (Hampson, 1986) or t^2-stretched CMP gather (Yilmaz, 1989).

Multiple suppression of the Radon transform is based on the velocity or moveout discriminations between primaries and multiples. From the definition of the Radon transform, events with different moveouts are mapped into focused points in different

regions in Radon space as illustrated by the semblance plot in Figure 2.8. Since primaries and non-associated multiples have different velocities, they can be separated from each other in Radon space. If multiples are muted in the Radon domain, multiple-free data can be reconstructed in the time-space domain; or if primaries are zeroed in the Radon domain and multiples reconstructed in the time-space domain and then subtracted from the original seismic data, multiple-free data are obtained. In practice, the latter approach is usually used to preserve amplitude versus offset information.

The details of the parabolic, hyperbolic and shifted-hyperbolic Radon transforms are discussed in Chapter 3.

Chapter Three: The Radon transform

3.1 Definition of the Radon transform

A few variations of the Radon transform have been explored in seismology including the parabolic Radon transform on NMO-corrected CMP gathers or common shot gathers (Hampson, 1986); the parabolic Radon transform on t^2-stretched CMP or common shot gathers (Yilmaz, 1989); the hyperbolic Radon transform on NMO-corrected CMP gathers (Foster and Mosher, 1992); the hyperbolic Radon transform on CMP or common shot gathers (Bancroft and Cao, 2004); and the shifted-hyperbolic Radon transform (Oppert, 2002; Oppert and Brown, 2002). Different types of Radon transform can also be applied over common scatter point gathers (Bancroft *et al*., 1998).

Hyperbolic Radon transform

A generalized formulation of the Radon transform is defined by Equation (2.5.2) in Chapter 2. A reflection point on a horizontal layer generates a hyperbolic event on a CMP gather (Figure 1.3). In order to map the hyperbolic event to a focused point in the Radon domain, the hyperbolic Radon transform over the CMP gather is defined as:

$$u(\tau, q) = \sum_{x} d\left(t = \sqrt{\tau^2 + qx^2}, x\right), \tag{3.1.1}$$

where $q = 1/v_{rms}^2$. The summation path is defined by $t = \sqrt{\tau^2 + qx^2}$, which implies a hyperbolic curve. Theoretically, this definition maps hyperbolic events in the time-space domain to a point in the Radon domain, as shown in Figure 3.1.

Because the multiple reflections have different velocities to those primary reflections which are not associated with the multiples, they are mapped to different

regions in the Radon domain and can be separated from each other. If multiples are muted in the Radon domain, multiple-free data can be reconstructed back to the time-space domain using the inverse Radon transform.

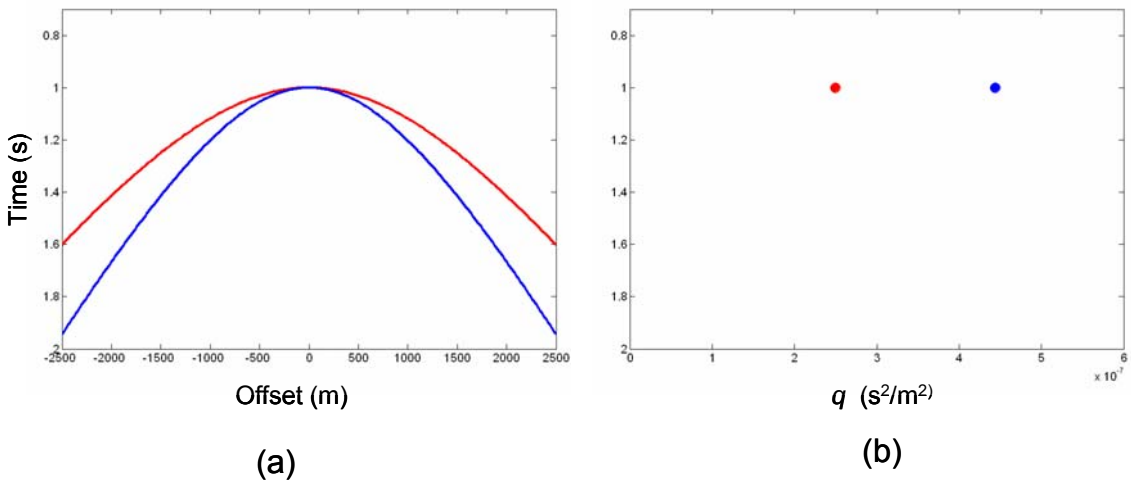

Figure 3.1 Hyperbolic events in the CMP domain (a) are mapped to focused points in the Radon domain (b) by the hyperbolic Radon transform.

Shifted-hyperbola Radon transform

In a horizontally layered model (Figure 1.5), Castle (1994) showed that Equation (1.1.3) is a small offset approximation to the actual response (Figure 3.2). The shifted-hyperbola equation was recommended by Castle as a solution to the inaccuracies of reflection moveout at longer offsets (Figure 3.3). The shifted-hyperbola equation proposed by Castle is defined as:

$$\left(t_{sh}-\tau_s\right)^2=\left(t_0-\tau_s\right)^2+\frac{x^2}{v_{sh}^2}, \tag{3.1.2}$$

where t_{sh} is the traveltime response of the shifted-hyperbolic moveout equation. The asymptotes of the shifted hyperbola will intersect at (x=0, t=τ_s) instead of (x=0, t=0). The

velocity information is now represented by v_{sh}. A more common form of the shifted-hyperbolic moveout equation is introduced by Castle (1994) as:

$$t = t_0\left(1-\frac{1}{S}\right)+\sqrt{\left(\frac{t_0}{S}\right)^2+\frac{x^2}{v_{sh}^2}}, \tag{3.1.3}$$

where

$$v_{sh}^2 = Sv_{rms}^2, \tag{3.1.4}$$

$$S = \frac{\mu_4}{\mu_2^2}, \tag{3.1.5}$$

and where

$$\mu_j = \frac{\sum_{k=1}^{N}\Delta\tau_k v_k^j}{\sum_{k=1}^{N}\Delta\tau_k}. \tag{3.1.6}$$

The shifted-hyperbola curve represents a Dix NMO equation shifted by the time $t_0\left(1-1/S\right)$. Equation (3.1.3) can now be written as:

$$t = t_0+\sqrt{\frac{t_0^2\mu_2^4}{\mu_4^2}+\frac{x^2\mu_2^2}{\mu_4 v_{rms}^2}}-\frac{t_0\mu_2^2}{\mu_4}. \tag{3.1.7}$$

Based on Equation (3.1.7), Oppert and Brown (2002) proposed the shifted-hyperbola Radon transform should match longer-offset reflection instead of the conventional Dix NMO Equation (1.1.3).

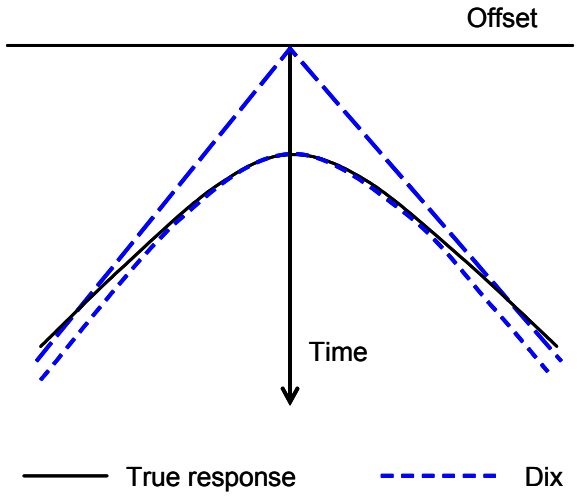

Figure 3.2 The non-hyperbolic reflection associated with a horizontally layered model as shown in Figure 1.5 and geometry of the Dix NMO equation (after Castle, 1994).

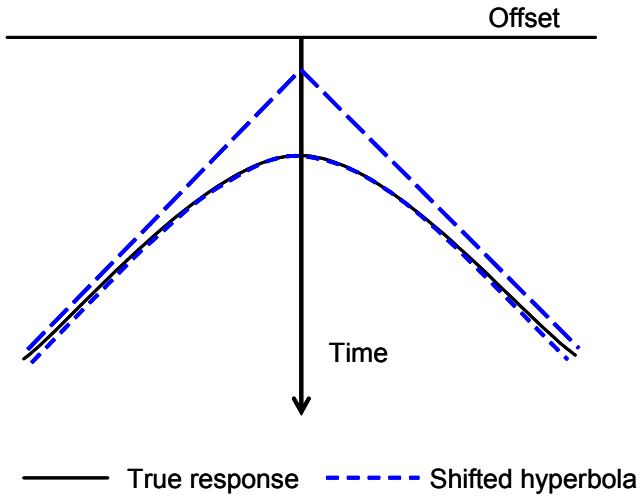

Figure 3.3 The non-hyperbolic reflection associated with a horizontally layered model as shown in Figure 1.5 and geometry of the shifted-hyperbola equation (after Castle, 1994).

Parabolic Radon transform

Hampson (1986) showed that multiple reflections on an NMO-corrected CMP gather can be approximately seen as parabolic. A parabolic Radon transform can then be

built on an NMO-corrected CMP gather by summing the data along the stacking paths defined by the equation $t = \tau + qx^2$. The reason to work on the parabolic Radon transform is explained in Section 3.3. An exact parabolic curve in the CMP domain can theoretically be mapped to a focused point in the parabolic Radon transform.

Consider an event with zero-offset two-way traveltime t_0 and RMS velocity v_{rms}. If this event is corrected with a velocity v_c, the event will now appear at time $T(x)$, where:

$$\begin{aligned} T(x) &= t_0 + \sqrt{t_0^2 + \frac{x^2}{v_{rms}^2}} - \sqrt{t_0^2 + \frac{x^2}{v_c^2}} \\ &= t_0\left(1 + \sqrt{1 + \frac{x^2}{v_{rms}^2 t_0^2}} - \sqrt{1 + \frac{x^2}{v_c^2 t_0^2}}\right) \end{aligned} . \tag{3.1.8}$$

Expanding Equation (3.1.8) in a Taylor series, we get

$$\begin{aligned} T(x) &= t_0\left(1 + \left(1 + \frac{1}{2}\frac{x^2}{v_{rms}^2 t_0^2} + \mathrm{L}\right) - \left(1 + \frac{1}{2}\frac{x^2}{v_c^2 t_0^2} + \mathrm{L}\right)\right) \\ &= t_0\left(1 + \frac{1}{2}\frac{x^2}{t_0^2}\left(\frac{1}{v_{rms}^2} - \frac{1}{v_c^2}\right) + \mathrm{L}\right) \end{aligned} . \tag{3.1.9}$$

A residual velocity v_r must be able to be found by:

$$\frac{1}{v_r^2} = \frac{1}{v_{rms}^2} - \frac{1}{v_c^2} . \tag{3.1.10}$$

Equation (3.1.10) can then be written as:

$$T(x) = t_0 + \frac{x^2}{2t_0 v_r^2} + \Lambda \quad ; \tag{3.1.11}$$

if $(x/(v_r t_0)) << 1$, the higher order terms can be dropped. Thus, to the extent that Equation (3.1.11) is valid, the NMO-corrected events on an input seismogram can be seen approximately as parabolae and be mapped to focused points in the Radon domain by:

$$u(\tau, q) = \sum_x d\left(t = \tau + qx^2, x\right), \tag{3.1.12}$$

with $q = 1/2t_0 v_r^2$.

As events deviate from the ideal parabolic form, amplitude smearing can be expected in the Radon domain and isolating events becomes harder. Yilmaz (1989) brought a different definition of the parabolic Radon transform which is defined over a t^2-stretched CMP or shot gather because a hyperbola in the CMP domain becomes an exact parabola after t^2-stretching the time axis. Consider events on a CMP gather with hyperbolic traveltimes defined by:

$$t^2 = t_0^2 + \frac{x^2}{v^2}. \tag{3.1.13}$$

Then, apply stretching in the time direction by setting $t' = t^2$ and $t_0' = t_0^2$. Equation (3.1.13) then takes the form:

$$t' = t_0' + \frac{x^2}{v^2}, \tag{3.1.14}$$

which is a definition of a parabola. So the parabolic Radon transform can be defined over the t^2-stretched CMP or shot gathers.

3.2 The Resolution problem of the Radon transform

We noted above that, theoretically, a hyperbolic event, for example, in the time-space domain, is mapped to a focused point in the Radon domain by the conventional

hyperbolic Radon transform as defined by Equation (3.1.1). However, in the real world, it doesn't work in this manner. Figure 3.4 (a) shows a hyperbolic event in the time-space domain and its Radon panel obtained by the conventional Radon transform. Notice the horizontal and oblique smearing energy in Figure 3.4 (b). The horizontal artifact is caused by the near-offset energy sharing and the oblique smearing by the far-offset truncation. Figure 3.5 shows that the integration paths associated with the same intercept time τ but different velocities or q are all sharing the event data at the near offsets in the CMP domain, which causes the horizontal smearing problem of the Radon transform. A data point at the zero-offset CMP gather shown in Figure 3.6 (a) is used to examine the near-offset artifacts of the forward Radon transform and the result is shown in Figure 3.6 (b) which looks like a horizontal event across the Radon panel. A CMP gather with a data point at the far offset shown in Figure 3.7 (a) is used to investigate far-offset artifacts. Its Radon panel shown in Figure 3.7 (b) explains the oblique artifacts in Figure 3.4 (b).

The smearing problem in the Radon domain decreases our ability to separate events, such as multiple energy from primary energy, in the Radon domain to attenuate multiples.

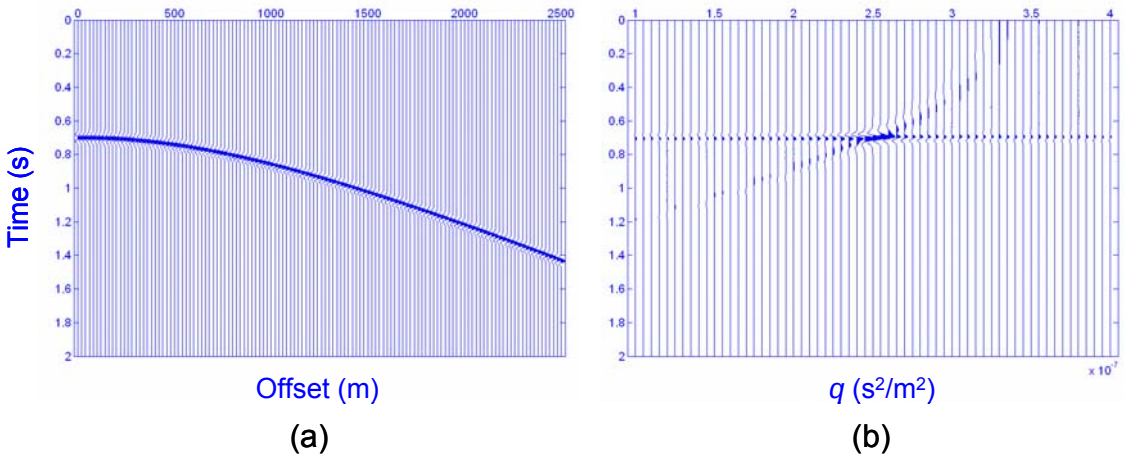

Figure 3.4 (a) A hyperbolic event in the time-space domain; and (b) its Radon panel by conventional hyperbolic Radon transform.

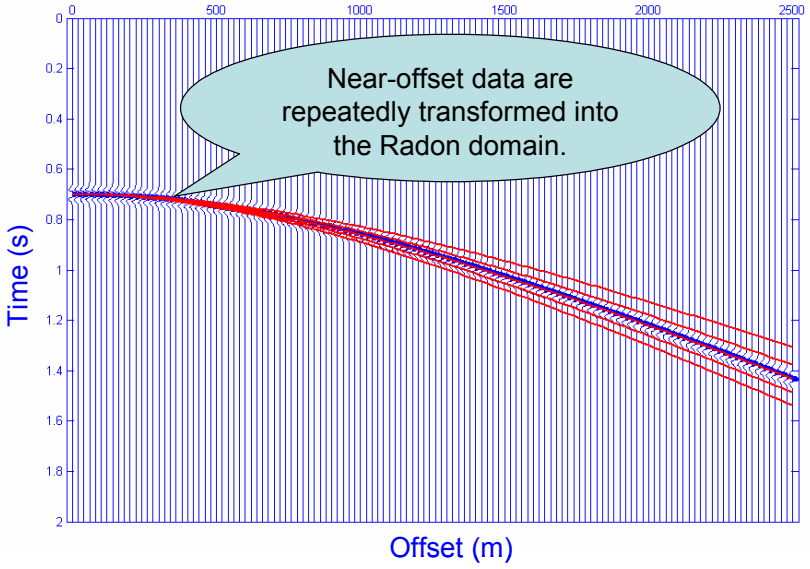

Figure 3.5 Near-offset data-sharing demonstration.

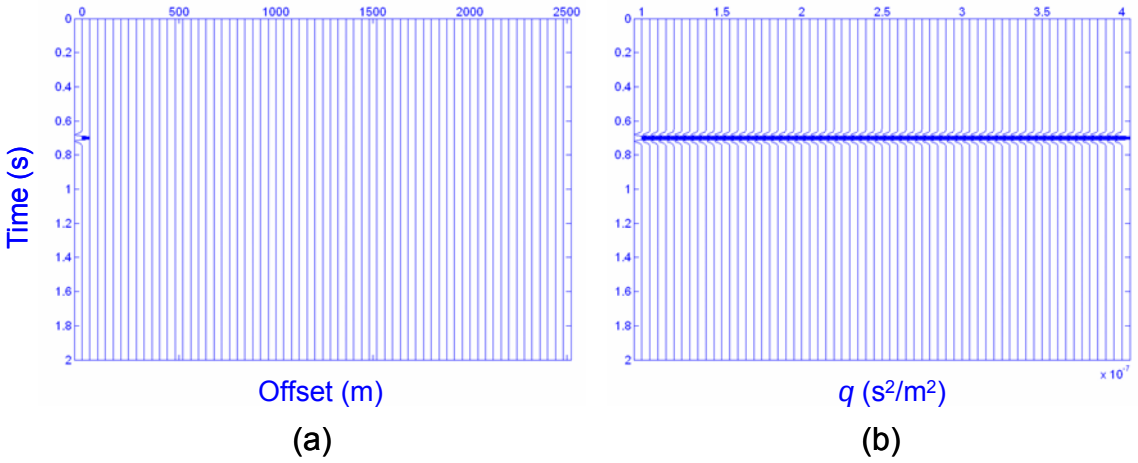

Figure 3.6 (a) A one-data-point CMP gather at zero-offset; and (b) its Radon panel.

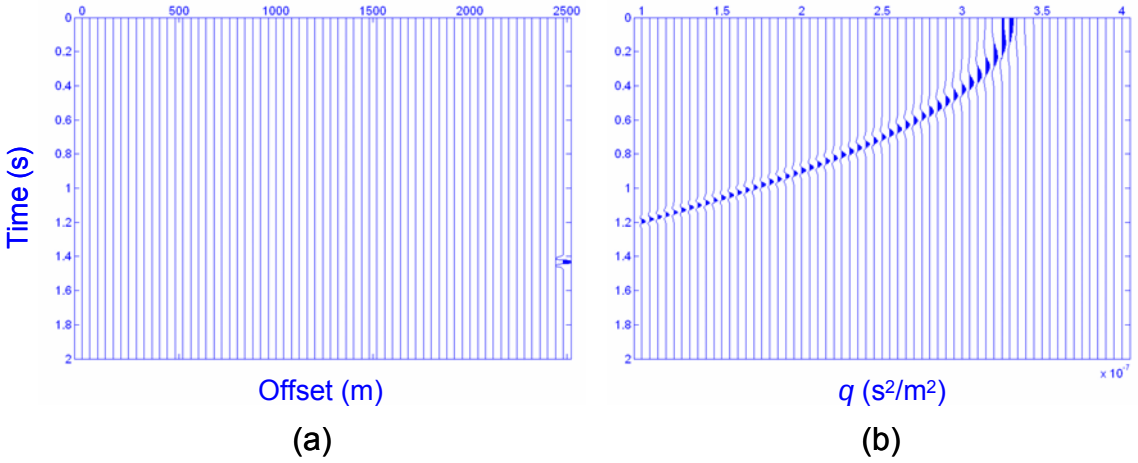

Figure 3.7 (a) A one-data-point CMP gather at the far offset; and (b) its Radon panel.

The dual operator of Equation (2.5.1) is:

$$d'(t,x)=\int_{-\infty}^{\infty}u\left(\tau=t-q\varphi(x),q\right)dq\ . \tag{3.2.1}$$

However, Beylkin (1987) showed that Equation (3.2.1) is not the inverse transform pair of Equation (2.5.1), which means if a model is forward Radon transformed into the Radon panel by Equation (2.5.1) and then inverse transformed by Equation (3.2.1), the reconstructed model is different from the original model. This can be explained by the example in Figure 3.4 and Figure 3.8. The Radon panel in Figure 3.4 (b) is obtained by forward Radon transforming the model in Figure 3.4 (a); the reconstructed time-space model in Figure 3.8 (a) is then obtained by inverse transforming the panel in Figure 3.4 (b) by Equation (3.2.1); continue to work on the forward and inverse Radon transform to generate the reconstructed time-space model shown in Figure 3.8 (c) and the Radon panel shown in Figure 3.8 (d). We can see from these figures that we keep losing energy in the time space models and decreasing the resolution in the Radon panel when keep working on the forward and inverse Radon transforms by Equations (2.5.1) and (3.2.1).

Beylkin (1987) found that the inverse integral transform pair of Equation (2.5.1) is defined by:

$$d'(t,x) = \int_{-\infty}^{\infty} \rho(\tau) * u(\tau = t - q\varphi(x), q)dq\,, \tag{3.2.2}$$

where $\rho(\tau)$ is called the *rho* filter and $*$ denotes convolution. For 2-D data, the *rho* filter $\rho(\tau)$ has a Fourier transform of the form $\sqrt{\omega}\,\mathbf{exp}(i\pi/4)$, where ω is the temporal frequency (Yilmaz, 2001). The dataset *d*′ (*t*,*x*) is the reconstruction of the time-space domain dataset from the Radon transform.

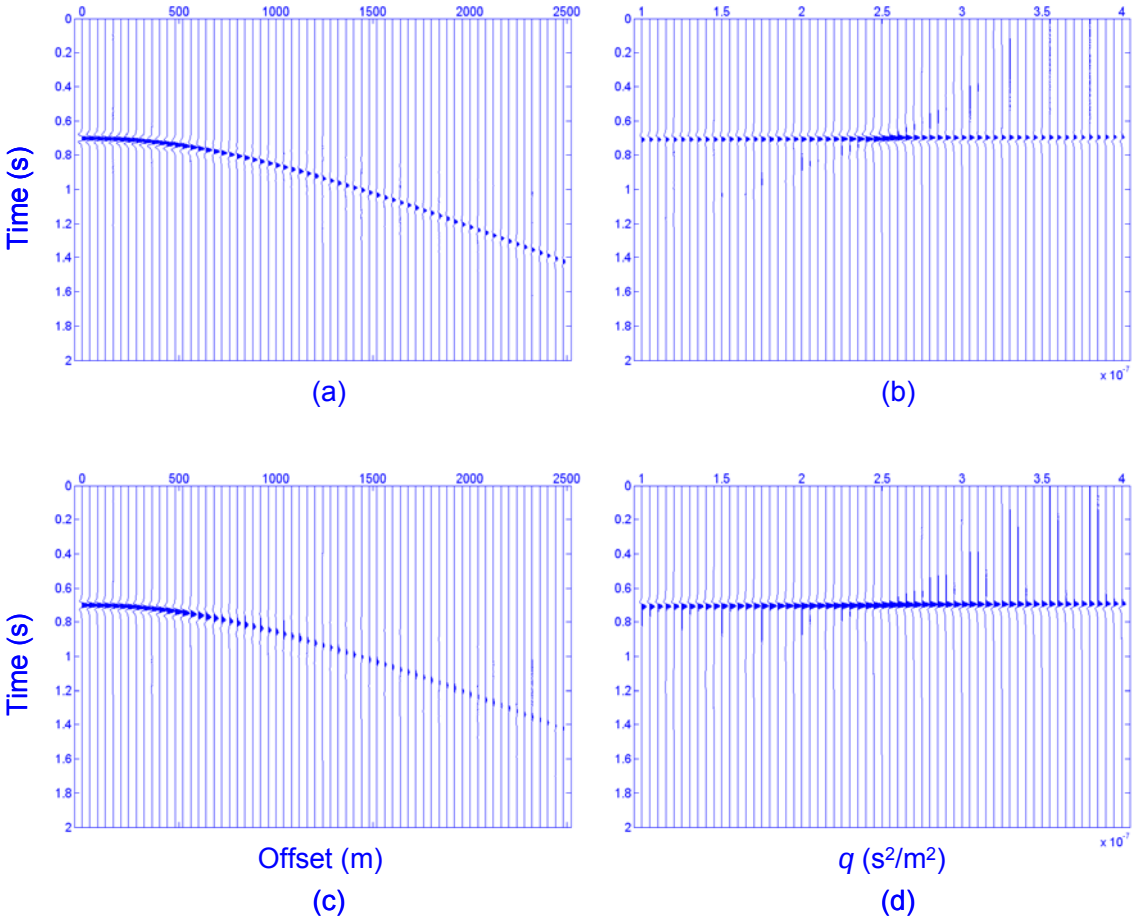

Figure 3.8 (a) The reconstructed hyperbolic event from Figure 3.4 (b); (b) the Radon panel of (a) by the conventional hyperbolic Radon transform; (c) The reconstructed event from (b); (d) the Radon panel of (c) by the conventional hyperbolic Radon transform.

3.3 Solutions to the Radon transform

Standard least-squares solution

In order to minimize the amplitude smearing on the conventional Radon panels, a least-squares formulation of the Radon methods was proposed by Thorson and Claerbout (1985) and Hampson (1986). Reverse mapping from the Radon domain back to the time-offset space in a discrete form of the continuous formula, Equation (3.2.1), becomes:

$$d'(t,x)=\sum_{q}u(\tau=t-q\varphi(x),q), \tag{3.3.1}$$

and its matrix form can be written as:

$$\mathbf{d}' = \mathbf{L}\mathbf{u}\,, \tag{3.3.2}$$

where $\mathbf{d}'$ stands for the reconstructed time-offset space data, $\mathbf{u}$ is a dataset in Radon space, and $\mathbf{L}$ is a linear operator defined by integrating the data in Radon space along the stacking paths $\tau = t - q\varphi(x)$. A matrix notation associated with Equation (2.5.2) (the forward Radon transform), with $\mathbf{L}^{\mathrm{T}}$ defined as a linear operator by integrating the data in the time-space domain along the stacking path $t = \tau - q\varphi(x)$, can be written as:

$$\mathbf{u} = \mathbf{L}^{\mathrm{T}}\mathbf{d}\,, \tag{3.3.3}$$

which is a low resolution solution to the Radon algorithms. Our purpose is to find an estimate of $u(\tau, q)$ with higher resolution, such that the difference $e(t, x)$ between the actual input gather $d(t, x)$ and the modelled time-offset space gather $d'(t, x)$ is minimal in the least-squares sense. The matrix notation of $e(t, x)$ is defined as (Yilmaz, 1989):

$$\mathbf{e} = \mathbf{d} - \mathbf{L}\mathbf{u}\,. \tag{3.3.4}$$

The least-squares solution for Equation (3.3.4) can be determined (Lines and Treitel, 1984). The cumulative squared error S is expressed as:

$$S = \mathbf{e}^{\mathrm{T}}\mathbf{e} = (\mathbf{d} - \mathbf{L}\mathbf{u})^{\mathrm{T}}(\mathbf{d} - \mathbf{L}\mathbf{u}), \tag{3.3.5}$$

where **T** donates matrix transposition. Minimizing *S* with respect to **u** gives the desired least-squares solution:

$$\mathbf{u} = (\mathbf{L}^{\mathrm{T}}\mathbf{L})^{-1}\mathbf{L}^{\mathrm{T}}\mathbf{d}\,, \tag{3.3.6}$$

where $\left(\mathbf{L}^{\mathrm{T}}\mathbf{L}\right)^{-1}\mathbf{L}^{\mathrm{T}}$ is the least-squares or generalized inverse of $\mathbf{L}$. Equation (3.3.6) is one form of the discrete Radon transform of $d(t,x)$ (Beylkin, 1987). To solve $u(\tau,q)$ using Equation (3.3.6) requires computing the inverse of $\mathbf{L}^{\mathrm{T}}\mathbf{L}$. It's impractical to invert this matrix due to the instability of the inversion, which is mostly caused by the non-uniqueness of the stacking paths at the near offsets of the input gather and discrete sampling over a finite range of offsets. Furthermore, although the operator $\mathbf{L}^{\mathrm{T}}\mathbf{L}$ is diagonally dominant, its side lobes are still significant which causes the smearing along the q-axis in the Radon domain.

A stable inversion approach was designed by Yilmaz (1989) by perturbing the matrix $\mathbf{L}^{\mathrm{T}}\mathbf{L}$ with a damping factor as follows:

$$\mathbf{u} = \left(\mathbf{L}^{\mathrm{T}}\mathbf{L} + \beta\mathbf{I}\right)^{-1}\mathbf{L}^{\mathrm{T}}\mathbf{d}\,, \tag{3.3.7}$$

where the constant β is the damping factor incorporated to add white noise along the diagonal of the operator $\mathbf{L}^{\mathrm{T}}\mathbf{L}$, and $\mathbf{I}$ is the identity matrix. In practice for field data, β is suggested to be 1% of the largest eigenvalue-squared of the operator $\mathbf{L}^{\mathrm{T}}\mathbf{L}$ (Yilmaz, 1989).

Frequency domain solution

However, it is impractical and very time consuming to invert the operator $\mathbf{L}^{\mathrm{T}}\mathbf{L}$ due to its large dimensions. Alternative solutions, to work on the parabolic Radon transform over NMO-corrected gathers or t^2-stretched gathers, were suggested by Hampson (1986) and Yilmaz (1989), respectively. Here I discuss why a parabolic Radon transform is applied even though events are not exactly parabolic on NMO-corrected CMP or shot gathers. The advantage of parabolic moveout over hyperbolic moveout is

that the traveltime moveout is invariant along the time axis for a specific value of velocity. The discrete form of Equation (3.3.1) defined over parabolic integration paths can be written as:

$$d'(t,x) = \sum_q u\left(\tau = t - qx^2, x\right). \tag{3.3.8}$$

By Fourier-transforming the time component of Equation (3.3.8), the moveout in the time axis becomes a phase shift in the frequency domain (Hampson, 1986 and Yilmaz, 1989):

$$d'(\omega,x) = \sum_q u(\omega,q)e^{-i\omega qx^2}, \tag{3.3.9}$$

where ω is the Fourier dual of t. Equation (3.3.9) can be written in the matrix form of (3.3.2) for each frequency component ω of $d'(\omega,x)$ and $u(\omega,x)$, where **L** now is a complex matrix of dimension $n \times k$:

$$\mathbf{L} = \begin{bmatrix} e^{-i\omega q_1 x_1^2} & e^{-i\omega q_2 x_1^2} & \mathrm{L} & e^{-i\omega q_k x_1^2} \\ e^{-i\omega q_1 x_2^2} & e^{-i\omega q_2 x_2^2} & \mathrm{L} & e^{-i\omega q_k x_2^2} \\ \mathrm{M} & \mathrm{M} & \mathrm{L} & \mathrm{M} \\ e^{-i\omega q_1 x_n^2} & e^{-i\omega q_2 x_n^2} & \mathrm{L} & e^{-i\omega q_k x_n^2} \end{bmatrix}, \tag{3.3.10}$$

and $\mathbf{d}'$ and **u** are complex vectors of lengths n, the number of offsets, and k, the number of q, respectively. The elements of the **L** matrix only depend on the geometry of the input gather, and the range of q used in constructing the Radon gather (Yilmaz, 1989). The constrained least-squares solution for **u**, i.e. Equation (3.3.6), now becomes:

$$\mathbf{u} = \left(\mathbf{L}^*\mathbf{L} + \beta\mathbf{I}\right)^{-1}\mathbf{L}^*\mathbf{d}, \tag{3.3.11}$$

where $*$ is the adjoint of **L**.

Because of the near-singular character of the complex matrix **L**, especially for small values of ω, the solution given by Equation (3.3.11) is best reformulated in terms of the singular value decomposition (SVD) of **L** (Press *et al*., 1986, and Yilmaz, 1989). **L** is factored into a product of three matrices (Lines and Treitel, 1984):

$$\mathbf{L} = \mathbf{U}\boldsymbol{\Lambda}\mathbf{V}^{*}, \tag{3.3.12}$$

where $\mathbf{U}$ and $\mathbf{V}$ are unitary matrices and $\boldsymbol{\Lambda}$ is a diagonal matrix whose elements are the singular values of the original matrix $\mathbf{L}$. By using this format of **L**, the constrained solution given by Equation (3.3.11) takes the form

$$\mathbf{u} = \mathbf{V}\left[\left(\boldsymbol{\Lambda}^{2} + \beta\mathbf{I}\right)^{-1}\boldsymbol{\Lambda}\right]\mathbf{U}^{*}\mathbf{d}, \tag{3.3.13}$$

where

$$\left(\boldsymbol{\Lambda}^{2} + \beta\mathbf{I}\right)^{-1}\boldsymbol{\Lambda} = \begin{bmatrix} \dfrac{\lambda_2}{\lambda_2^2+\beta} & & & 0 \\ & \dfrac{\lambda_2}{\lambda_2^2+\beta} & & \\ & & \mathrm{O} & \\ 0 & & & \dfrac{\lambda_2}{\lambda_2^2+\beta} \end{bmatrix}, \tag{3.3.14}$$

and λ_i are the positive square-roots of the eigenvalues λ_i^2 of $\mathbf{L}^{*}\mathbf{L}$.

Kostov (1990) showed that the term $\left(\mathbf{L}^{\mathrm{T}^{*}}\mathbf{L} + \beta\mathbf{I}\right)$ in Equation (3.3.11), the least-squares solution of the Radon transform, has a Toeplitz structure even for data that are irregularly sampled or non-uniformly weighted in offset. Solving the inverse of this Toeplitz matrix using the Levinson recursion is computationally efficient.

High-resolution solution in the frequency domain

The constant regularization parameter, β, provides an inexact approximation of events outside the finite aperture range of the data, subsequently smearing energy along the *q*-axis. A variable regularization term is required to constrain the smearing problem of the transform in a data-dependent manner. Sacchi and Ulrych (1995) proposed a high-resolution technique that involves an iterative method of employing the data within the sparsity constraint to allow for a better resolution in the transform domain.

The initial estimation of the transform data $\mathbf{u}$ obtained by Equation (3.3.11) is used to determine the regularization parameter to minimize the smearing problems along the *q*-axis in the high-resolution method. The non-constant diagonal regularization matrix, $\mathbf{D}(\mathbf{u}_k)$, replaces $\beta\mathbf{I}$ in Equation (3.3.11) and is defined for each iteration as:

$$\mathbf{D}(\mathbf{u}_k) = \frac{\alpha\mathbf{I}}{b + |u_i^2|}, \tag{3.3.15}$$

where u_i denotes elements of the vector $\mathbf{u}_k$, and the constant parameters, α and *b*, are optimized for a CMP gather prior to application to the entire dataset. The parameter *b* is included in the damping factor to provide for white noise and may be alternatively estimated as 1% of the maximum of $|u_i^2|$, while the parameter β may be substituted for α (Oppert, 2002). A quantile of $\mathbf{u}_k$ was recommended by Trad *et al*. (2003) for the parameter *b*. The *p* quantile of $\mathbf{u}_k$ is the value of $\mathbf{u}_k$ where its cumulative distribution takes the value *p*. The elements of the matrix $\mathbf{D}(\mathbf{u}_k)$ are basically inversely proportional to the 'energy' of the model estimated from the previous preliminary transform. The

diagonal matrix $\mathbf{D}(\mathbf{u}_k)$ is computed during each iteration of the high-resolution transform and the transform is determined as follows:

$$\mathbf{u}_{k+1} = \left(\mathbf{L}^{\mathrm{T}^*}\mathbf{L} + \mathbf{D}(\mathbf{u}_k)\right)^{-1} \mathbf{L}^{\mathrm{T}^*}\mathbf{d}\,, \tag{3.3.16}$$

where $\mathbf{u}_k$ is the model solution at the k^{th} iteration. Typically three iterations are necessary to provide an optimally constrained solution.

However, the term $\left(\mathbf{L}^{\mathrm{T}^*}\mathbf{L} + \mathbf{D}\right)$ in Equation (3.3.16) doesn't have a Toeplitz structure since the main diagonal elements of the regularization matrix **D** are not constant. The fast Levinson algorithm suggested by Kostov (1990) can't be employed to invert the matrix $\left(\mathbf{L}^{\mathrm{T}^*}\mathbf{L} + \mathbf{D}\right)$. Alternatively, Sacchi and Porsani (1999) proposed a method to achieve an effective high-resolution Radon solution, by means of conjugate gradients, at a cost comparable to the conventional parabolic least-squares solution computed with the Levinson recursive solution.

Cary (1998) pointed out that imposing a sparseness constraint only in the q direction is a necessary but insufficient condition for a desirable solution to resolve closely spaced events. In this case, sparseness constraints in both the τ and q directions are required to employ a slower time-domain algorithm, which was the stochastic method proposed by Thorson and Claerbout (1985) in the time domain. In the stochastic method, a non-linear sparse solution in both τ and q directions can be achieved by using the ratio of the noise variance to the Radon space **u** variance instead of a constant damping factor, $\beta\mathbf{I}$ in Equation (3.3.7). A time domain high-resolution Radon solution can be written as:

$$\mathbf{u}_{k+1} = \left(\mathbf{L}^{\mathrm{T}}\mathbf{L} + \mathbf{D}\left(\mathbf{u}_k\right)\right)^{-1}\mathbf{L}^{\mathrm{T}}\mathbf{d}\,, \tag{3.3.17}$$

where $\mathbf{u}_k$ is the Radon solution at the k^{th} iteration. The initial solution $\mathbf{u}_0$ is estimated by the standard least-squares solution shown as Equation (3.3.7).

Semblance-weighted Radon method

Bradshaw and Ng (1987, unpublished) worked on the parabolic semblance-weighted Radon transform with the Gauss-Seidel iterative method in the time domain. Yilmaz and Taner (1994) used a similar method in the least-squares sense to compute the slant-stack.

The weight function, semblance, was defined by Stoffa *et al*. (1981). Semblance can be written as follows along parabolic trajectories:

$$S\left(\tau, q\right) = \frac{\sum_{l}\left(\sum_{x} d\left(t = \tau + qx^2, x\right)\right)^2}{N_x \sum_{l}\sum_{x} d^2\left(t = \tau + qx^2, x\right)}, \tag{3.3.18}$$

where l is a window size and is usually a wavelet length, and N_x is the number of traces in the time-space domain involved in the semblance calculation. Semblance has the important property that its value is only dependent on the coherency of events and independent of the amplitudes of the input dataset; it ranges from 0 to 1, indicating poorest to best fit of the proposed trajectory respectively (Bradshaw and Ng, 1987). Weighting the forward Radon transform with semblance can enhance energy cluster along those trajectories which fit seismic events well in the seismic dataset while weakening energy along those trajectories which badly fit seismic events. Applied in the

Gauss-Seidel sense, the semblance-weighted Radon approach produces moderately high-resolution results. The weighted parabolic Radon transform is then defined as follows:

$$u(\tau,q)=S(\tau,q)\sum_{x} d\left(t=\tau+qx^2,x\right). \tag{3.3.19}$$

The semblance plot of the model in Figure 3.4 (a) is shown in Figure 3.9 and the Radon panel computed by Equation (3.3.19) is shown in Figure 3.10. Comparing the Radon panel in Figure 3.10 and the panel in Figure 3.4 (b), the former gives more focused energy in the Radon domain.

According to Bradshaw and Ng (1987) and Ng and Perz (2004), the following steps describe one single Gauss-Seidel iteration:

(a) Given a particular value of $q=q_i$, stack the input gather $\mathbf{d}_k$ (k is the iteration number and the initial input is the original dataset **d**) along the proposed trajectory q_i; calculate the semblance of the gather along this trajectory; weight and threshold the stack with the semblance. This gives an estimate $u_{est}(\tau,q_i)$ at this q_i trace.

(b) Compute the inverse Radon transform $\mathbf{d}_k^{'}$ at this q_i trace and subtract it from the current input gather to create a new dataset $\mathbf{d}_{k+1}$, which is called residual gather and will be the new input dataset to calculate the Radon transform along another trajectory q_{i+1}. The input energy gradually diminishes as the calculation proceeds and the Gauss-Seidel iterations increase.

(c) Add the current estimate at q_i trace, $u_{est}(\tau,q_i)$, to the accumulated estimate in the transform domain, $u_{acc}(\tau,q_i)$.

(d) Increment to the next q trace, q_{i+1}, and repeat steps (a) to (d) until all q traces are covered. The only difference is that the input dataset in step (a) now will be the residual dataset $\mathbf{d}_{k+1}$ obtained in step (b).

Typically, three passes of the Gauss-Seidel iterations of steps (a)-(d) are sufficient to reduce the *t*-*x* domain residual energy below an acceptable level (Ng and Perz, 2004). After the first iteration, replace the weight function, semblance, by a constant function (since the residual energy can be very weak in subsequent iterations), so that the residual errors will be gradually removed and stabilized as iterations proceed. After three Gauss-Seidel iterations, the estimate $u_{acc}(\tau, q)$ is obtained and constitutes the forward Radon transform.

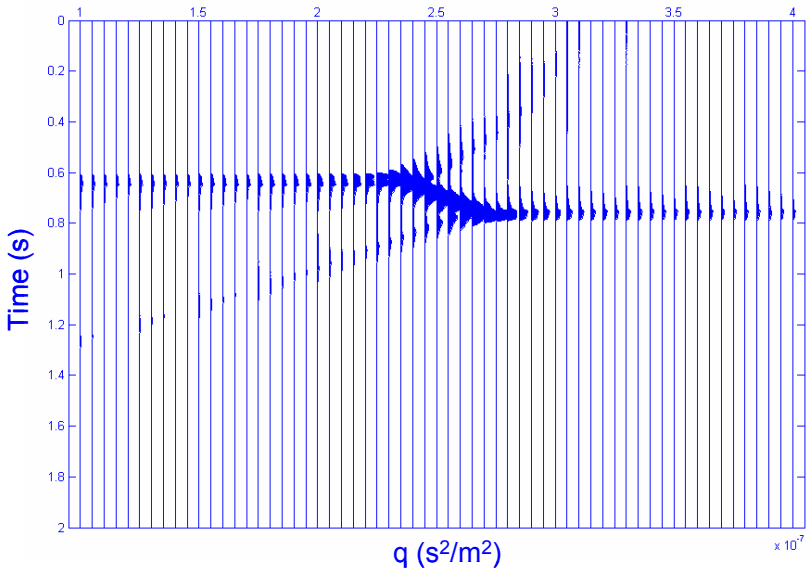

Figure 3.9 The semblance plot of the model in Figure 3.4 (a).

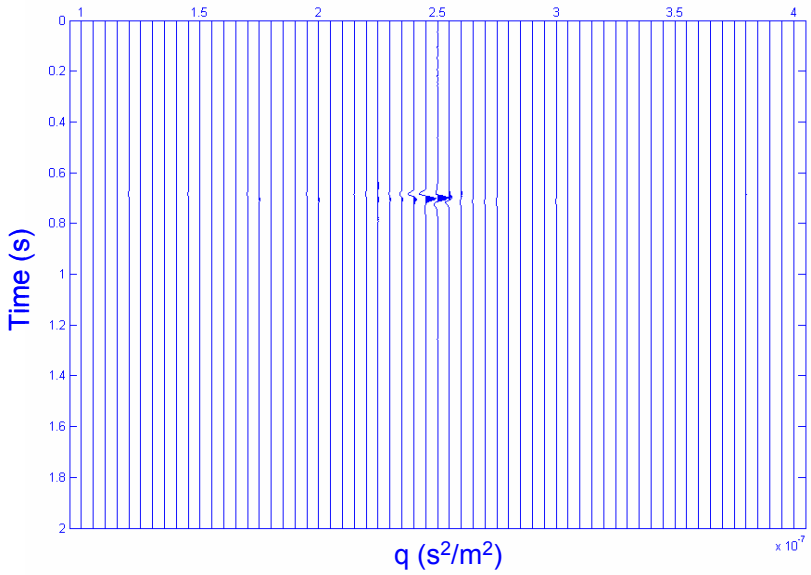

Figure 3.10 The Radon panel of the model in Figure 3.4 (a) obtained by the semblance-weighted Radon solution (scaled to Figure 3.4 (b)).

The optimized semblance-weighted Radon solution

A new high-resolution time domain semblance-weighted Radon solution using the Gauss-Seidel scheme was proposed by Ng and Perz (2004). In order to utilize the previous transform as a priori information in the current transform to achieve sparseness in a Gauss-Seidel scheme, a well-known property of the Gauss-Seidel algorithm should be discussed. For early iterations in the algorithm, the model energy tends to reside in whichever model components are estimated first. The Gauss-Seidel calculation of the semblance-weighted method is based on a sequential q index, which leads to energy preference to those q traces which are estimated first. The results from the semblance-weighted method are then used to estimate the power of q and a new sequence of q traces is generated. A new process of semblance-weighted Radon transform now starts over from step (a) to step (d) using the current q-estimation sequence. The initial input gather is still the original t-x CMP gather. This scheme ensures that the most significant q traces

are estimated first and contain the strongest energy, which leads to a solution sparse in the q direction. Optionally, the current transform becomes the new preliminary results for a revised q-estimation sequence and the process is repeated.

In order to demonstrate the algorithm strategy that the optimized semblance-weighted Radon transform adopts, a model is shown in Figure 3.11 with its 5 tentative Radon transform stacking trajectories, from top to down, with corresponding to Trace 1, 2, 3, 4 and 5 respectively in Figure 3.12, which shows an enlarged portion of the Radon panel of the model. The true velocity of the event corresponds to Trace 3, which stands for a perfect fit trajectory of the event in Figure 3.11. Once the initial Radon model, Figure 3.12, is obtained by the semblance-weighted Radon transform, the energy along the q-axis can be estimated, which is indicated in Figure 3.12 by a trapezoid. Apparently, Trace 3 has the highest energy accumulation among all the traces.

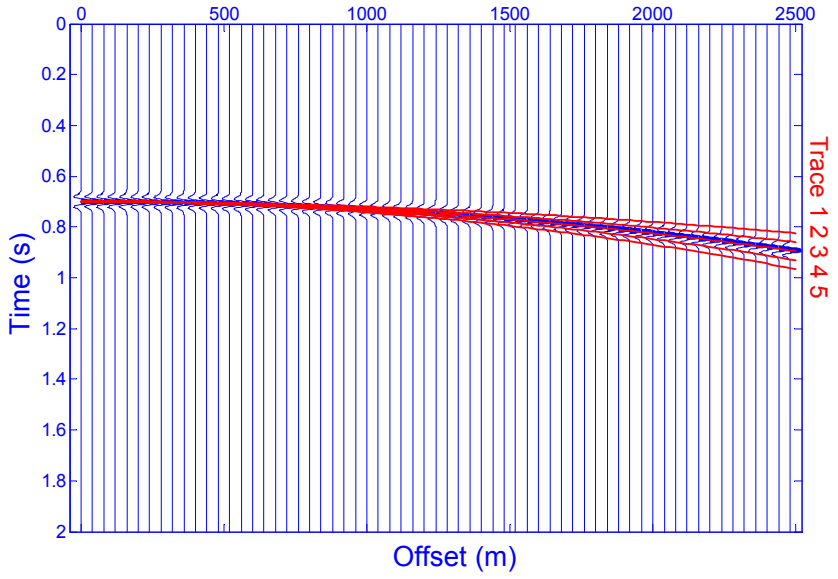

Figure 3.11 A model with 5 tentative stacking trajectories.

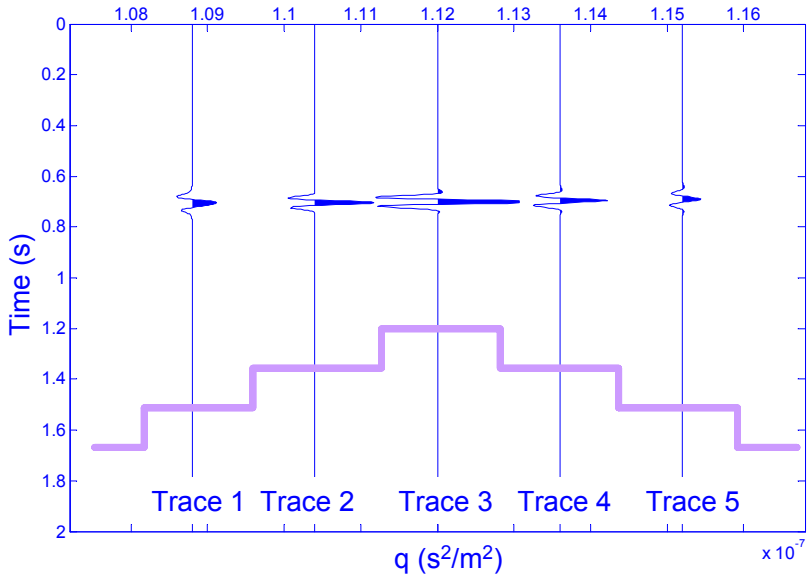

Figure 3.12 A small portion of the Radon transform of the model in Figure 3.11.

The second iteration of the optimized semblance-weighted algorithm will be first employed over Trace 3 and the Radon panel obtained is shown in Figure 3.13. The data which are already transformed into the Radon space are then removed from the input gather, and the residual gather, shown in Figure 3.14, will be the new input data for the next q trace, which in this case could be Trace 2 or 4.

Since the trajectory of Trace 3 is a perfect fit of the event, there is not much energy left after the first run over Trace 3. When we move to the next q trace, there is not much smearing energy that can be brought in (Figure 3.15) to the Radon domain. If the threshold mentioned in step (a) of the semblance-weighted Radon transform is used, the smearing energy can be controlled at a more limited level.

The procedure of the Gauss-Seidel iterations of the optimized semblance-weighted Radon solution is summarized as follows:

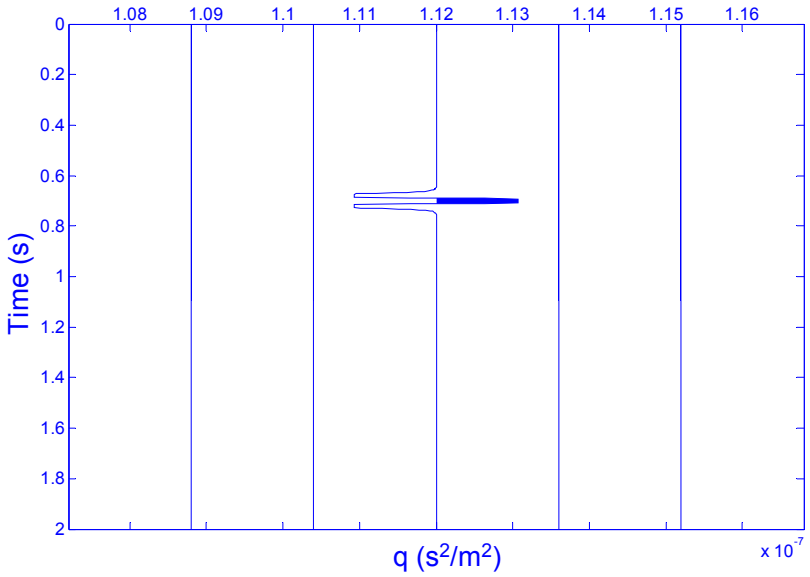

Figure 3.13 The Radon panel of the model obtained by working on Trace 3.

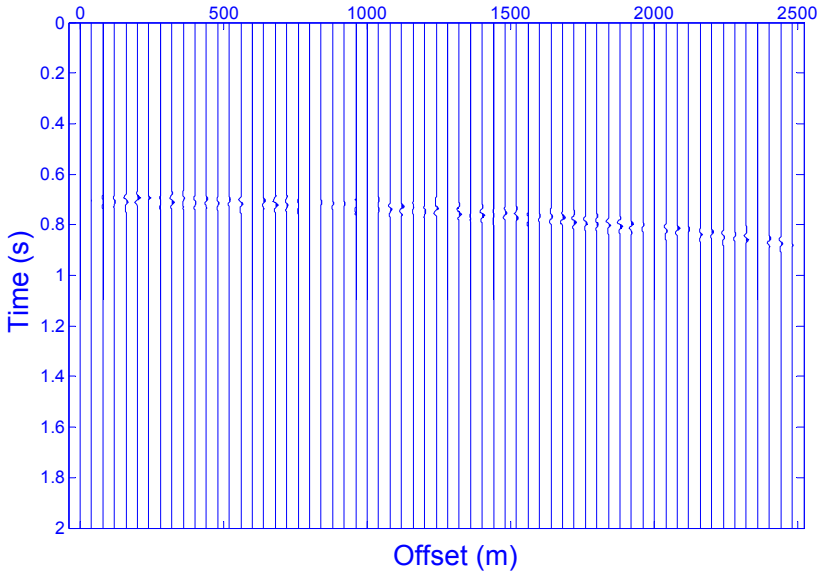

Figure 3.14 The updated input data after the data along Trace 3 that have been transformed into the Radon space are removed from the original input data.

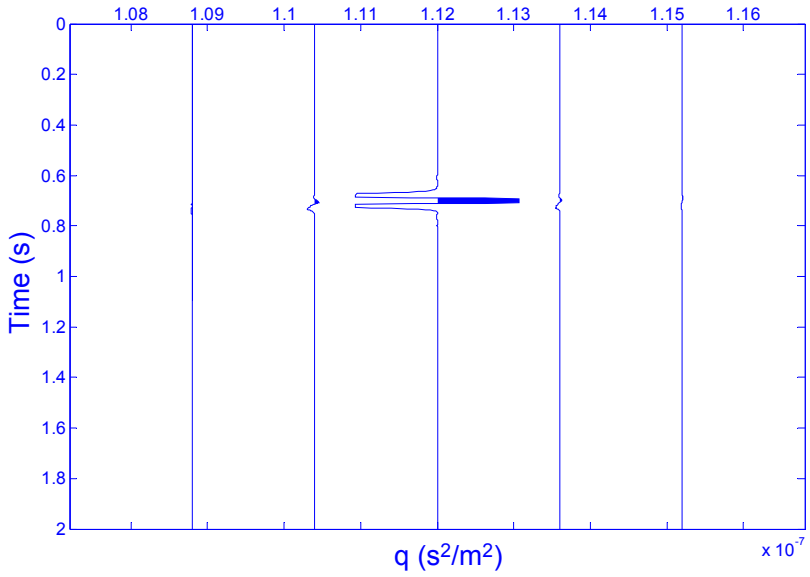

Figure 3.15 The final Radon panel of the model in Figure 3.11 by the optimized semblance-weighted Radon solution.

(a) Calculate the Radon panel, $\mathbf{u}_1$, of the input gather $\mathbf{d}$ according the steps of the semblance-weighted Radon method as described in the section of ***Semblance-weighted Radon method***.

(b) Sort the q sequence based on energy cluster of $\mathbf{u}_1$ in a descending power.

(c) Start from q_i=q_1, then increment to q_2, q_3, … according to the q sequence obtained in step (b), to stack the input gather $\mathbf{d}_k$ (k is the iteration number and the initial input is the original dataset $\mathbf{d}$) along the proposed trajectory q_i; calculate the semblance of the gather along this trajectory; weight and threshold the stack with the semblance. This gives an estimate $u_{est}(\tau, q_i)$ at this q_i trace.

(d) Compute the inverse Radon transform $\mathbf{d}_k^{'}$ at this q_i trace and subtract it from the current input gather $\mathbf{d}_k$ to create a new dataset $\mathbf{d}_{k+1}$, which is called residual gather

and will be the new input dataset to calculate the Radon transform along the next trajectory q_{i+1}. The input energy gradually diminishes as the calculation proceeds and the Gauss-Seidel iterations increase.

(e) Add the current estimate at q_i trace, $u_{est}(\tau, q_i)$, to the accumulated estimate in the transform domain, $u_{acc}(\tau, q_i)$.

(f) Increment to the next q trace, q_{i+1}, based on the q sequence and repeat steps (c) to (e) until all q traces are covered. The only difference is that the input dataset in step (c) now will be the residual dataset $\mathbf{d}_{k+1}$ obtained in step (b).

3.4 Stacking path analysis

A precondition of the high-resolution Radon methods is using reasonably accurate stacking paths. The more closely the stacking path matches the moveout of events, the better the separation of multiples from primaries in Radon space. Parabolic and hyperbolic paths are commonly used for the Radon transform in exploration seismology. In order to implement a fast computation algorithm in the frequency domain, Hampson (1986) developed a DRT (discrete Radon transform) algorithm along the parabolic trajectories on NMO-corrected CMP gathers. However, after NMO-correction, multiple events are not exactly parabolic. Foster and Mosher (1992) showed that the residual moveout of multiples on a CMP gather after NMO-correction is closer to a hyperbola rather than a parabola. The hyperbolic stacking path focusing events reflected from depth z_{ref} is defined by:

$$t = \tau + q\left(\sqrt{x^2 + z_{ref}^2} - z_{ref}\right). \tag{3.4.1}$$

As mentioned above, for a layered-earth model (Figure 1.5), the interval velocity of each layer varies, mostly increases, with depth. The moveout Equation (1.1.3) of seismic events which is in use throughout the industry today, is approximately hyperbolic only at small offsets and gradually deviates from the hyperbola at far offsets as shown in Figure 3.2 (Taner and Koehler, 1969). In this case the shifted-hyperbola moveout Equation (3.1.3) can be used as an alternative to build the Radon transform stacking paths, as shown in Equation (3.1.7).

3.5 Analysis of aliasing

Data aliasing and operator aliasing are involved in seismic data processing. Data aliasing is caused by under-sampling a signal with respect to the Nyquist frequency either along the time or space direction (Trad, 2001).

Turner (1990) analyzed data aliasing in both the time and p axes of the linear Radon transform. Aliasing in the time direction is governed by the same rule as time sampling in the time-space:

$$\Delta\tau \le \frac{1}{2f_{ny}}, \tag{3.5.1}$$

where $\Delta\tau$ is the sampling rate of the time axis and f_{ny} stands for the Nyquist frequency. Aliasing in the p direction is governed by:

$$\Delta p \le \frac{1}{f_{ny}\left(x_{\max} - x_{\min}\right)}, \tag{3.5.2}$$

where $x_{\max}$ and $x_{\min}$ are the maximum and minimum offsets, respectively, in the time-space domain, and Δp is the sampling rate in the slant-stack domain (Turner, 1990, and

Trad, 2001). The parabolic Radon transform can be regarded as a linear Radon transform after an x^2 stretch in the time-space domain (Hugonnet and Canadas, 1995). So the critical sampling interval of the parabolic Radon transform is determined by:

$$\Delta q \le \frac{1}{f_{ny}\left(x_{\max}^2 - x_{\min}^2\right)}. \tag{3.5.3}$$

The sampling interval in the offset direction of the time-space domain of the linear Radon transform is given by (Turner, 1990):

$$\Delta x \le \frac{1}{f_{ny}\left(p_{\max} - p_{\min}\right)}. \tag{3.5.4}$$

After the variable transform of $x \Rightarrow x^2$ and $\Delta x \Rightarrow 2x\Delta x$ is applied, the Δx requirement for the parabolic Radon transform can be determined:

$$\Delta x \le \frac{1}{2f_{ny}\left|x\right|_{\max}\left(q_{\max} - q_{\min}\right)}. \tag{3.5.5}$$

Cary (1998) and Trad (2001) both pointed out that the aliasing problem of the Radon transform is also associated with the use of the operator. When a continuous function $d\left(x,t\right)$ is sampled, its discrete function doesn't fully represent the data in the continuous field and the sinc function operator has to be applied to its discrete form to fully reconstruct the information and prevent aliasing:

$$d\left(x,t\right) = \sum_t \sum_x d\left(x_i, t_j\right) Sinc\left(\frac{t - t_j}{\Delta t}\right) Sinc\left(\frac{x - x_i}{\Delta x}\right), \tag{3.5.6}$$

where Δt and Δx are the Nyquist sample rates along the time and space directions, respectively.

Chapter Four: Application of different Radon methods

4.1 Synthetic data examples of the Radon transforms

This chapter is devoted to comparing different Radon algorithms through their application on a synthetic dataset. The synthetic NMO-corrected CMP gather shown in Figure 4.1 contains offsets from 0 to 2500 m and the trace interval is 20 m. Two primaries, Pa and Pb, with constant amplitudes across the offsets, flat after NMO correction, are located at 0.3 s and 0.57 s respectively. One of the five multiple events in parabolic shapes, Ma, has the same traveltime as Pa at zero offset and its moveout at the far offset is 20 ms. Notice from Figure 4.2, an enlarged portion of Figure 4.1, that Ma is very close to Pa and they are difficult to differentiate. They are partially mixed with each other even at far offsets and there is only 20 ms between their peaks at the farthest offset. Mb, with a zero offset traveltime of 0.5 s and moveout of 70 ms at the far offset, overlaps the primary Pb at far offsets. Mc is located at 0.7 s at zero offset. This event has uniform amplitudes and is not interfered with by any other event. Md, with a vertical traveltime of 1.02 s and a moveout of 120 ms at the far offset, has variable amplitudes at the near offsets; and Me, with a vertical traveltime of 1.3 s and a moveout of 150 ms at the far offset, shows variable amplitude effects at far offsets.

The least-squares solution to the Radon transform in the frequency domain shown in Equation (3.3.6) is examined first. The optimum value of the damping factor, β, which is related to the noise level in the input dataset and guarantees the stability of inversion in Equation (3.3.11) (Yilmaz, 1989), is selected to be 1% of the largest eigenvalue of the operator $\mathbf{L}^{\mathbf{T}^*}\mathbf{L}$, λ_1^2, to compute the Radon panel of the CMP gather shown in Figure 4.1

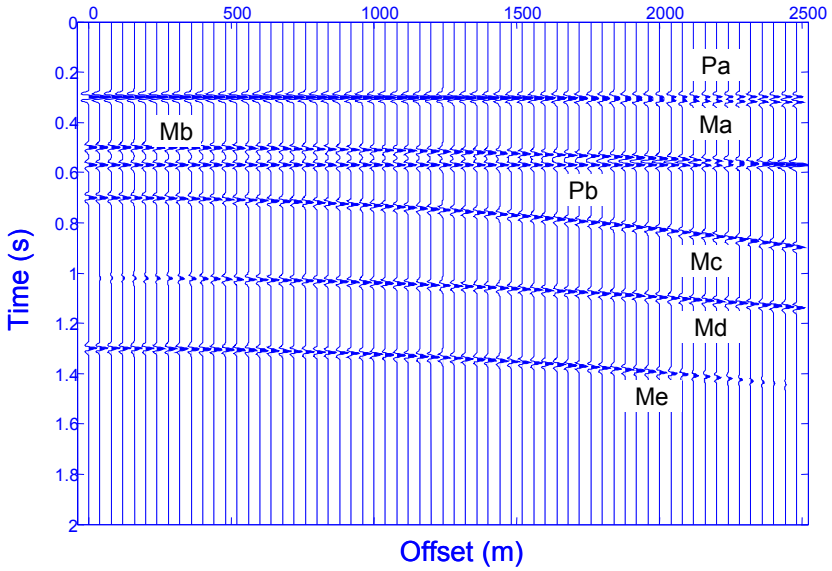

Figure 4.1 A synthetic NMO-corrected CMP gather including two primaries Pa and Pb and five multiples Ma, Mb, Mc, Md and Me.

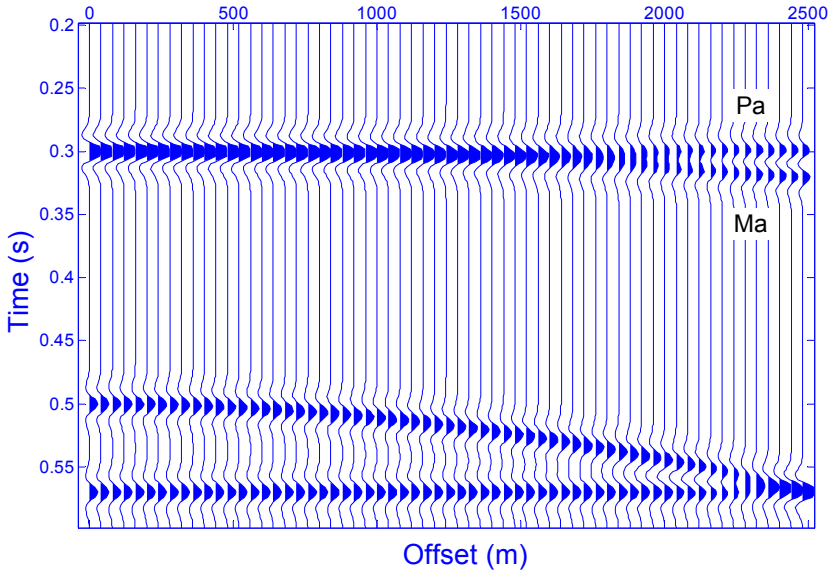

Figure 4.2 An enlarged portion of the model in Figure 4.1. Notice that Pa and Ma are hard to separate even though they are enlarged.

and the reconstructed CMP gather. The results are shown in Figure 4.3: (a) the model; (b) the Radon panel; (c) the reconstructed gather from the Radon panel using Equation (3.2.1); and (d) the residual gather which is obtained by subtracting the reconstructed gather from the original model. The Figures (c) and (d) are scaled to figure (a). All events are smeared in the Radon panel. The smear across the q-axis horizontally indicated by S_q is caused by energy sharing at the near offsets and the oblique smear indicated by S_τ is caused by far-offset energy sharing. In particular, events Pa and Ma are smeared together because the moveouts between the two events are too small and it is impossible to differentiate them.

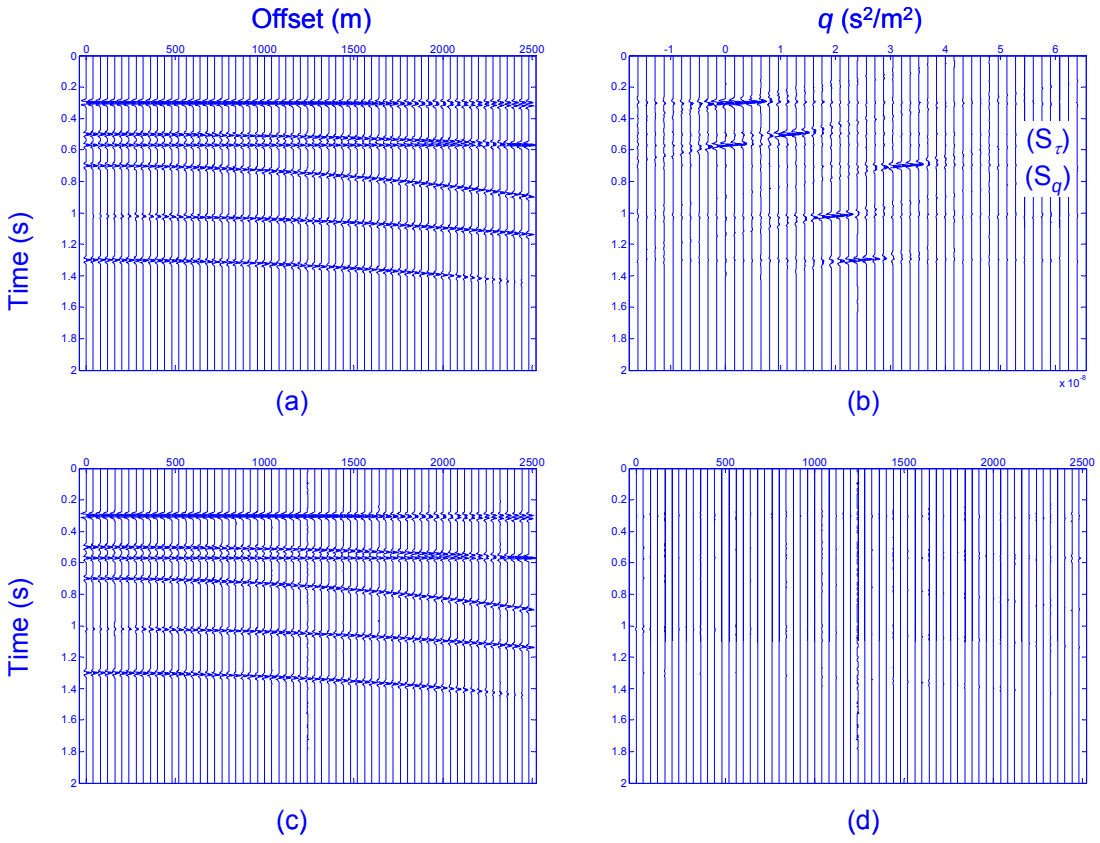

Figure 4.3 Results of the least-squares solution: (a) the model; (b) the Radon panel; (c) the reconstructed gather; and (d) the residual gather by subtracting (c) from (a).

The high-resolution frequency domain solution proposed by Sacchi and Ulrych (1995) is then applied to the model. The first iteration of the high-resolution Radon solution involves the same damping factor as the least-squares solution: i.e., the previous results from the least-squares method (Figure 4.3 (b)) are used to compute the high-resolution Radon panel in the following iterations. The damping factor in the iterations other than the first one, the matrix **D** in Equation (3.3.16), is determined by the Radon results from the previous iteration, as defined by Equation (3.3.15), for sparsity constraints in the q direction. The use of the adaptive damping factor **D** intends to eliminate the smear across the q-axis. The amount of sparsity imposed on the operator is limited by the regularization parameters, α and b (Oppert, 2002). If large values are used for the factor α, the matrix $\left(\mathbf{L}^{\mathbf{T}^*}\mathbf{L}+\mathbf{D}\right)^{-1}$ is diagonally dominant and sharp distributions between events and background noise in the model will be created (Sacchi and Ulrych, 1995 and Oppert, 2002). The background power b stabilizes the damping factor **D** when $\mathbf{u}_i$ approaches zero. In order to avoid the tedious computation to get the regularization parameters, Oppert (2002) suggested the parameter b be equal to 1% of the maximum value of $\left|\mathbf{u}_i^2\right|$, which is the transformed data from the previous iteration, and α be 0.01% to 1% of the maximum of the main diagonal of the operator matrix $\mathbf{L}^{\mathbf{T}^*}\mathbf{L}$. Trad *et al*. (2003) proposed the use of a quantile of $\left|\mathbf{u}_i^2\right|$ to estimate the constant regularization b and 1 is used for α in Equation (3.3.15). In this example, the 70% quantile of $\left|\mathbf{u}_i^2\right|$ is used for b. The results are shown in Figure 4.4.

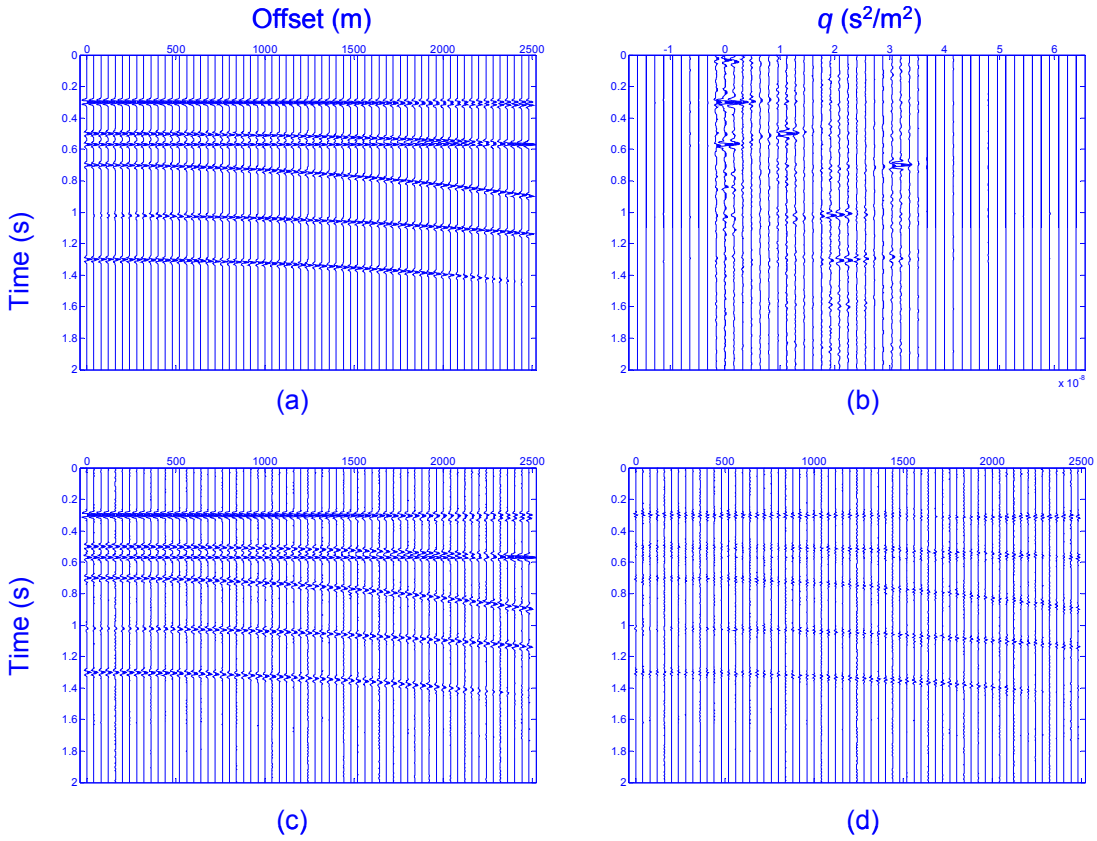

Figure 4.4 Results of the high-resolution method: (a) the model; (b) the Radon panel; (c) the reconstructed gather; and (d) the residual gather by subtracting (c) from (a).

Comparing Figure 4.3 (c-d) and Figure 4.4 (c-d) shows that the conventional least-squares solution gives more exact reconstruction, which is the way the least-squares solution is designed, than the high-resolution algorithm. The residual gather Figure 4.3 (d) calculated by subtracting the reconstructed gather (c) from the original input CMP gather (a) is only random noise. The drawback of the high-resolution solution is that it destroys the reconstruction of the original data, which can be verified by Figure 4.4 (d) where the residual events can be clearly seen. Comparing Figure 4.3 (b) and Figure 4.4 (b), the high-resolution method produced more focused events in the Radon panel. One important observation from Figure 4.4 (b) is that there is energy leakage along the time axis within

the q range of about $0\sim3.5\times10^{-8}$ s^2/m^2. This is because the sparsity solution in the frequency domain is only constrained in the q direction, not along the time axis. Even though the high-resolution method obviously compressed the events much more than the least-squares method, event Ma can't be separated from event Pa.

The results of the Gauss-Seidel iterative semblance-weighted Radon method introduced by Bradshaw and Ng (1987) are shown in Figure 4.5. Compared to the least-squares solution and the frequency domain high-resolution method, the forward Radon panel calculated by this method in Figure 4.5 (b) is further improved. The smear in both τ and q directions are obviously reduced and there is no sign of the energy leakage that the frequency domain high-resolution method shows due to its employment in the time domain. The utilization of semblance information defined by Equation (3.3.18) in the weighting function of the Radon transform, Equation (3.3.19), results in the sparsity constraints. The Gauss-Seidel iterative method also attempts to minimize the smearing problem by removing the transformed energy from the original input dataset for each q trace during calculation. However, the event Ma can not yet be separated from the event Pa even though this method resulted in fairly good resolution in the Radon panel. The reconstructed CMP gather shown in Figure 4.5 and the residual energy in Figure 4.5 (d) show that reconstruction with minimal errors is obtainable by this method.

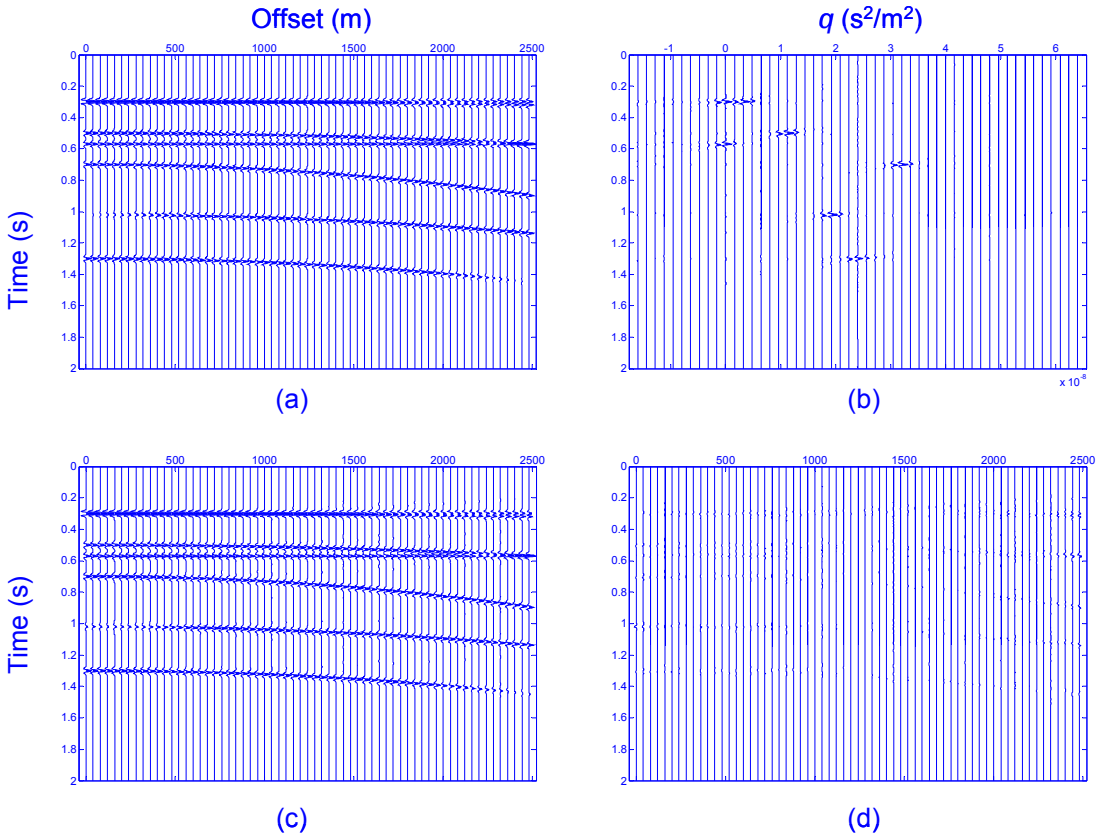

Figure 4.5 Results of the semblance-weighted Radon method: (a) the model; (b) the Radon panel; (c) the reconstructed gather; and (d) the residual gather.

Even though Figure 4.5 (b) shows impressive results in the Radon panel, it is not perfect. The philosophy of the Gauss-Seidel method is that for early iterations, most of the energy in the data space, or in the CMP gather in this case, resides in whichever model components are estimated first (Ng and Perz, 2004). This is the reason why the Gauss-Seidel method still produces smearing energy in the Radon panel. During the implementation of the Gauss-Seidel algorithm, the calculation is performed based on sequential q traces. The energy is first taken by the earlier q traces, which can be explained using the example in Figure 4.6. For the model in Figure 4.6 (a), there are two tentative q traces, q_1 and q_2, with the latter as the best fit of the event in the gather, as

shown in Figure 4.6 (a). The Radon transform is first performed over q_1 and then q_2. After the Gauss-Seidel algorithm for the Radon transform is performed over q_1, some of the data along this trace are stacked into the Radon panel as shown in Figure 4.6 (b), which stands for the smearing energy, and are then removed from the input dataset. The residual dataset is shown in Figure 4.6 (c). The model in (c) loses some data compared to the model in (a). When the computation is moved to the trace q_2, which stands for the perfect fit of the event trajectory as we mentioned, the input data model is now incomplete. Therefore, the final Radon panel obtained by the algorithm shown in Figure 4.6 (d) is biased.

The analysis of the Gauss-Seidel algorithm performed on the model in Figure 4.6 above led us to think about performing the algorithm first over the trace q_2 rather than q_1. If the transform is first estimated along the trajectories which best fit the events in the CMP gather, most of energy in the model would be stacked into the positions defined by these trajectories or q traces and the smear in Figure 4.5 (b) could be further reduced. This is the so-called optimized semblance-weighted Radon transform (Ng and Perz, 2004). It's suggested that the distribution information of the Radon panel along the q-axis be estimated from the preliminary result in Figure 4.5 (b), calculated by the Gauss-Seidel iterative method, and a sequence in the sense of descending power of q is set up. The new Gauss-Seidel scheme is employed using the new q sequence, which suggests that the Radon transform is first estimated along the most important trajectories, or the trajectories best describing the events in the data space. This implementation in turn leads to a solution sparse in both the q-axis and the time direction (Ng and Perz, 2004). The result of the model in Figure 4.6 (a) using this optimized semblance-weighted Radon

algorithm is shown in Figure 4.7. We can see that the wiggle is not biased and there is very limited smear information on the trace q_1.

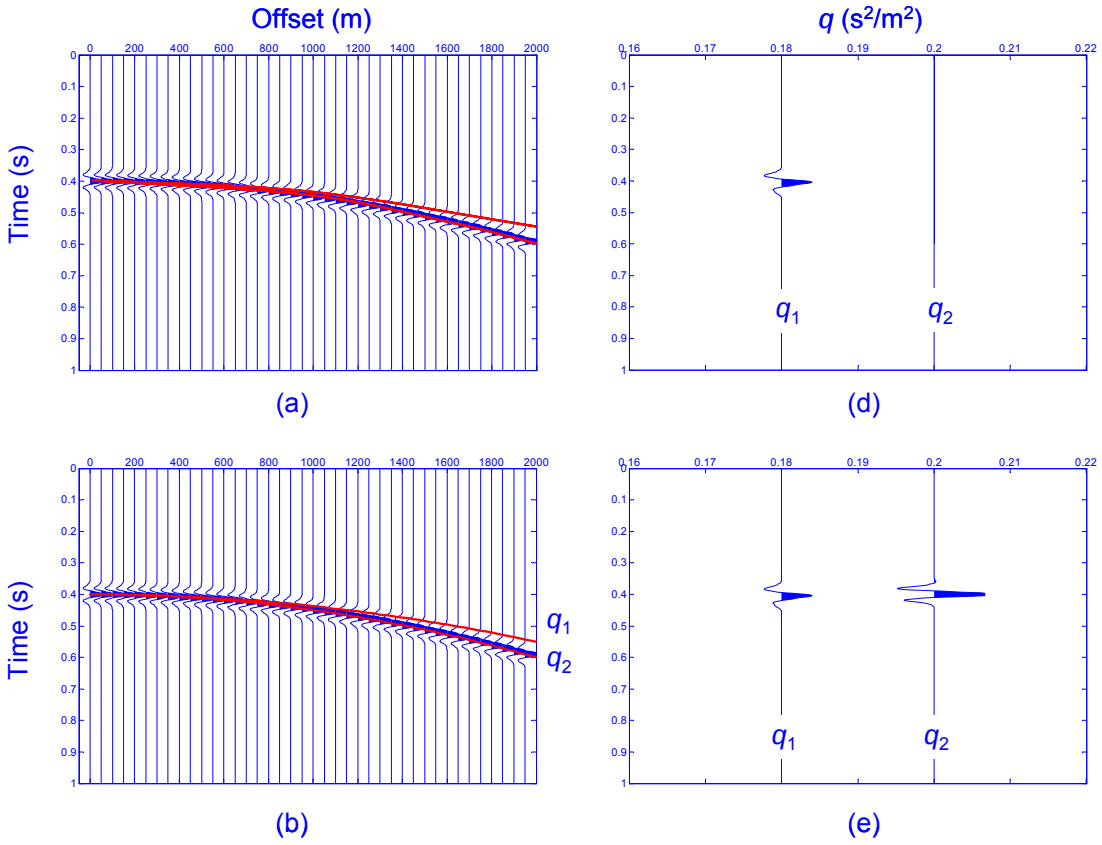

Figure 4.6 The Gauss-Seidel algorithm: (a) a CMP model with two tentative q traces; (b) the Radon panel obtained after the Gauss-Seidel Radon transform is performed over q_1; (c) the residual input model after the Gauss-Seidel Radon method is performed over $q1$; and (d) the Radon panel obtained by performing the algorithm over q_1 and q_2.

The results of the optimized Gauss-Seidel semblance-weighted Radon transform of the model in Figure 4.1 are shown in Figure 4.8. The Radon panel in Figure 4.8 (b) is very impressive in that the events Pa and Ma can be clearly separated from each other even though there is only a 20 ms interval between the peaks of them at the farthest offset. The reconstruction of the CMP gather shown in Figure 4.8 (c) and the residual energy shown in (d) indicate a very good reconstruction.

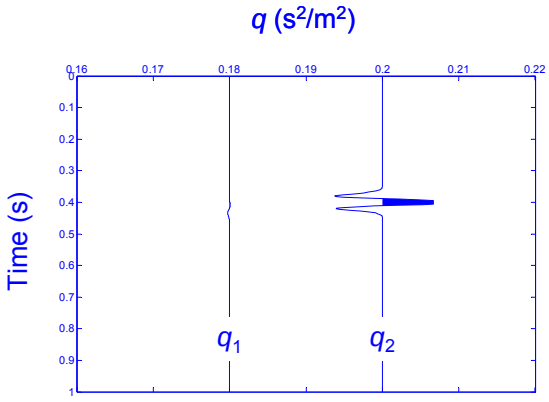

Figure 4.7 The Radon panel of the model in Figure 4.6 (a) obtained by performing the optimized semblance-weighted Radon algorithm.

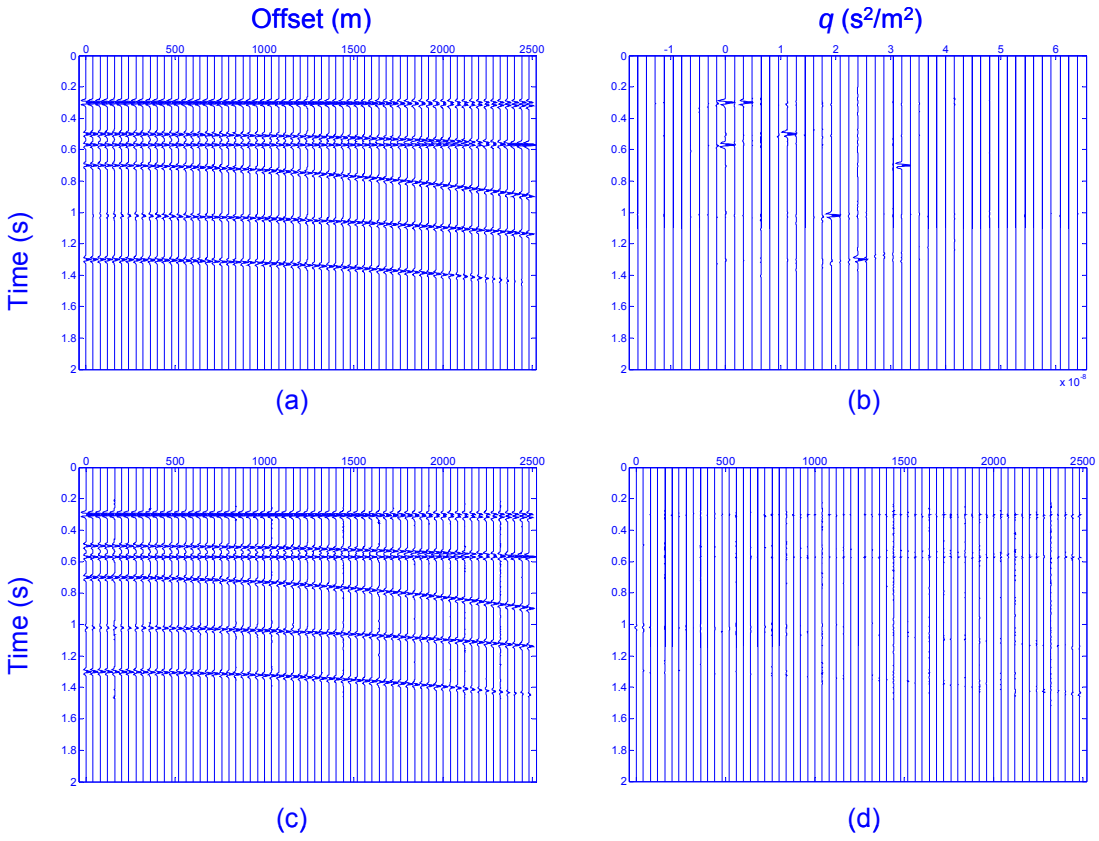

Figure 4.8 Results of the optimized semblance-weighted Radon method: (a) the model; (b) the Radon panel; (c) the reconstructed gather; and (d) the residual gather.

In this example, the input CMP gather in Figure 4.1 is NMO-corrected before the Radon analysis. In the case of a CMP gather without NMO-correction, the t^2-stretching scheme proposed by Yilmaz (1989) can be employed to implement the parabolic Radon technique since a hyperbola becomes a parabola exactly after square stretching along the t-axis. However, in practice, the NMO-corrected CMP gather is preferred because the non-corrected gather has distinctly larger moveout than the corrected gather. The algorithm is much more expensive if it is applied on the non-corrected gather rather than the corrected one since a larger range of q traces have to be adopted.

In order to test the resolution of the different algorithms in the Radon panel without being effected by the stacking path pattern, the events in the synthetic CMP gather shown in Figure 4.1 are designed to be exactly parabolic. This is not true in real seismology even though the events on the CMP gather are exactly hyperbolic before NMO-correction; they are approximately parabolic after the correction. However, the utilization of parabolic events demonstrated the success of the different algorithms on the Radon transform analysis.

Another feature of the synthetic dataset is that the wavelet used is identical at all times and offsets. In real data, the wavelet is stretched by NMO correction. Consequently the synthetic data will show more optimistic view of the high resolution Radon transform. For real datasets, stretch effect is usually muted after NMO correction.

4.2 Real data example

The White Rose oilfield is located offshore Newfoundland on the east coast of Canada. The water depth there is about 120 m. Due to the hard water-bottom, high ocean-

bottom reflection coefficients create strong water-column reverberations in this area. High impedance contrast also occurs at the Tertiary-Cretaceous unconformity, which causes serious peg-leg multiple problems. Underlying this Tertiary-Cretaceous unconformity is the target reservoir, the Avalon sandstone formation, which is strongly affected by the peg-leg multiples.

The CMP gather in this area shown in Figure 4.9 has been chosen to illustrate the serious multiple problems. From the figure, we can easily see the water-column reverberations above the reflection of the Tertiary-Cretaceous unconformity at about 2.2 s, and the peg-leg multiples of this reflector below 2.2 s with a periodicity of about 0.16 s. The strong multiples can also be recognized from the semblance plot of this CMP gather in Figure 4.10. The semblance plot also shows that there is a much weaker primary event located at about 2.7 s overlain by the strong peg-leg multiples of the Tertiary-Cretaceous unconformity. This reflection will be very hard to interpret on a stack section.

We have concluded that a faster computation of the Radon transform can be achieved by performing the algorithm on an NMO-corrected gather rather than an original gather since the NMO-corrected gather has smaller moveouts. The NMO-corrected version of the CMP gather in Figure 4.9 is shown in Figure 4.11 based on the velocity analysis in Figure 4.10. This NMO-corrected gather is used to perform the optimized semblance-weighted Radon method and the obtained Radon panel is shown in Figure 4.12. The full reconstruction of the Radon panel back into the time-space domain and the residual gather which is the difference between the full reconstructed gather from the original gather are shown in Figure 4.13 and Figure 4.14, respectively. The residual

gather is only random noise and shows very minor amplitudes compared to Figure 4.9 and Figure 4.13. The success of the optimized semblance-weighted Radon method is again verified on the real data example by the two figures, Figure 4.13 and Figure 4.14.

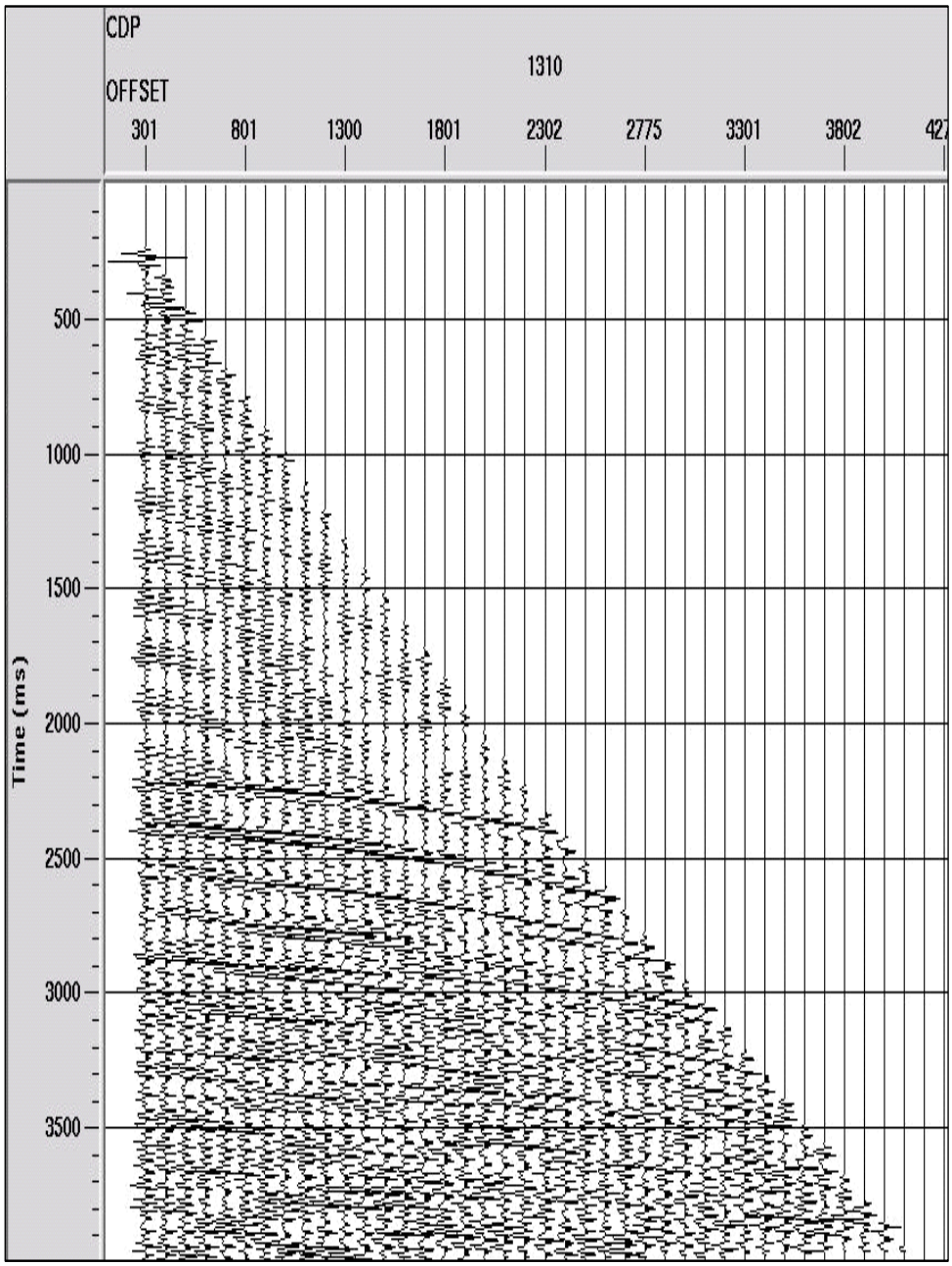

Figure 4.9 The original CMP gather.

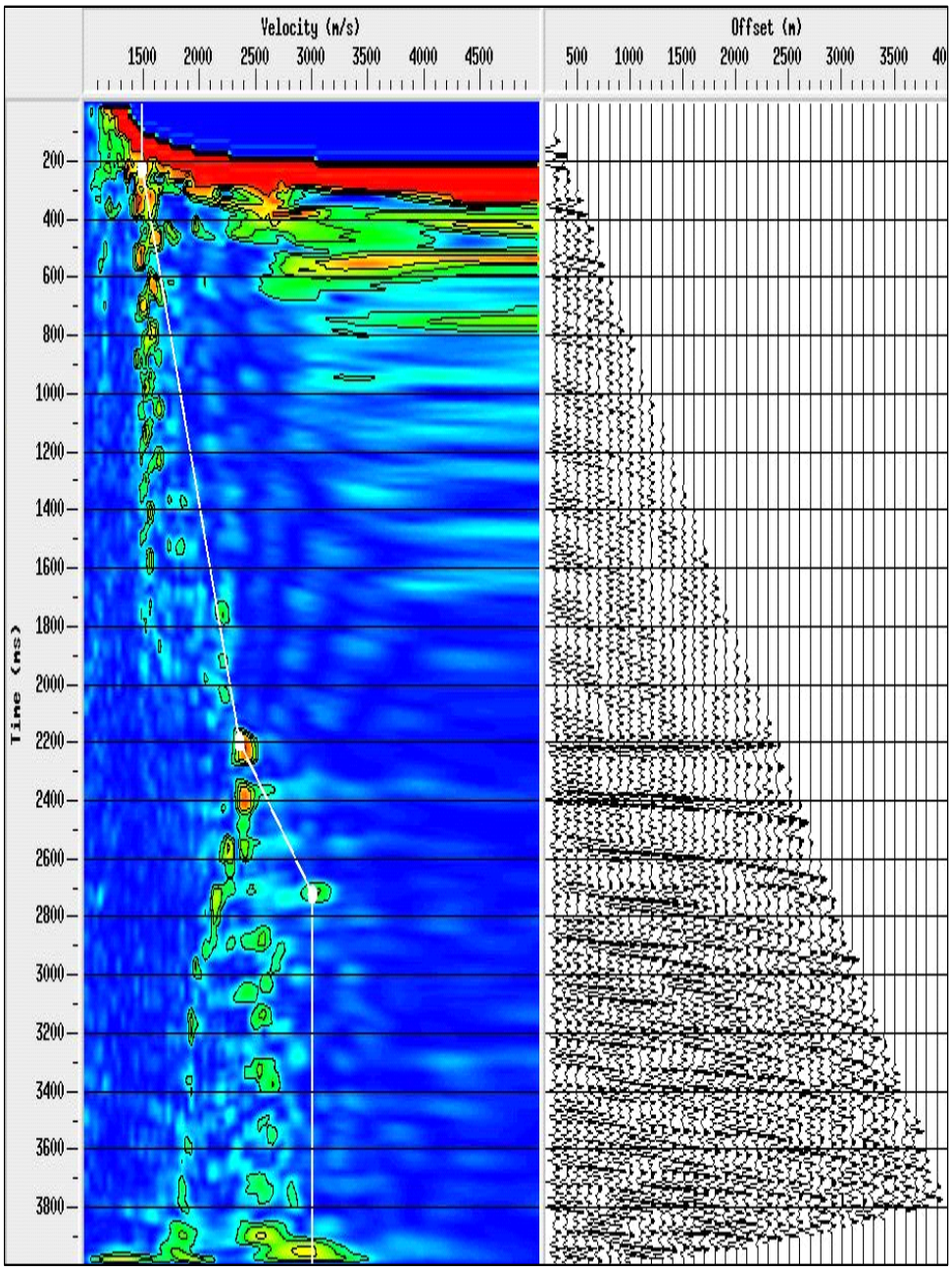

Figure 4.10 The semblance plot of the CMP gather in Figure 4.9.

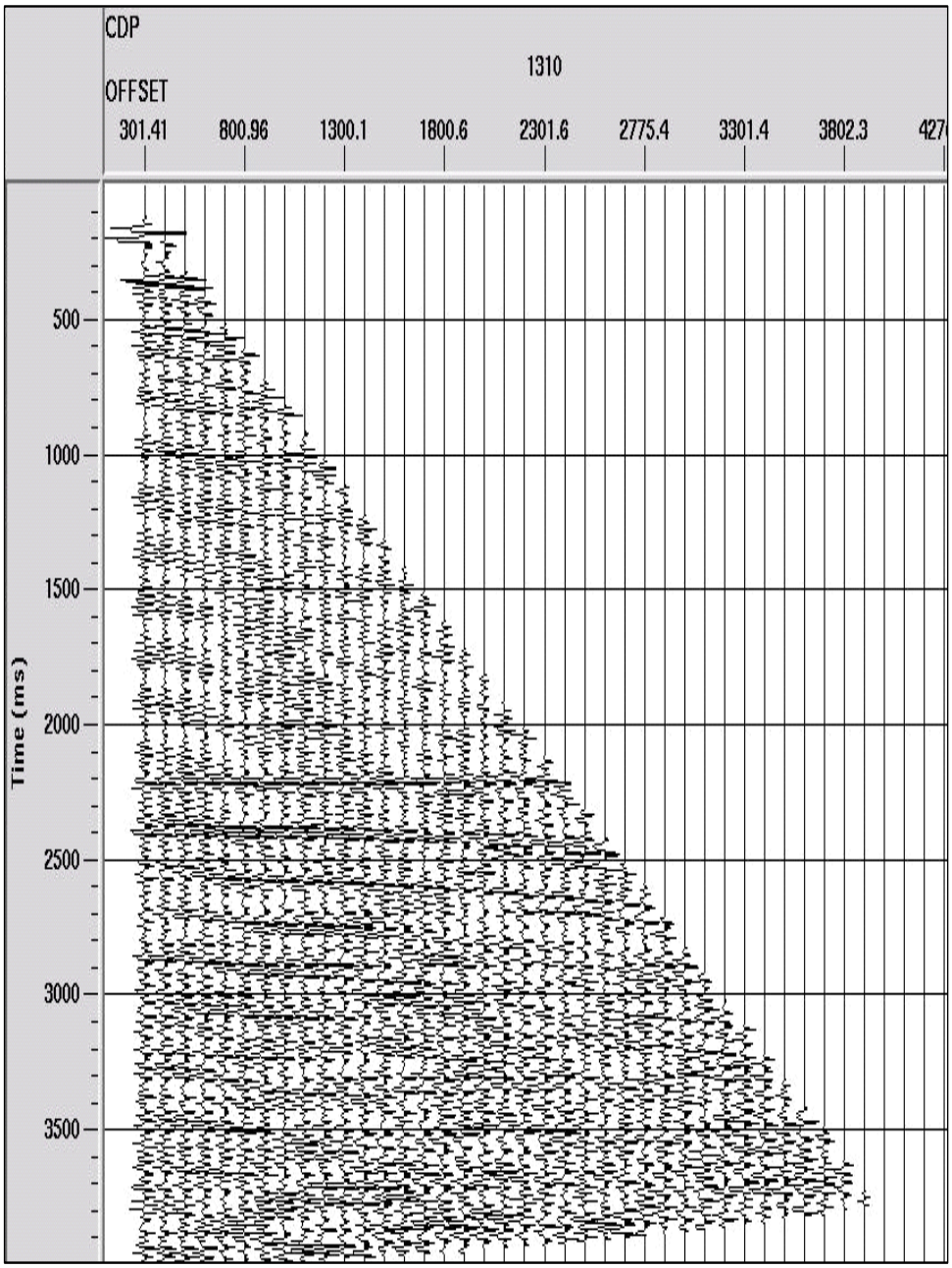

Figure 4.11 The NMO-corrected CMP gather. (Scaled to Figure 4.9)

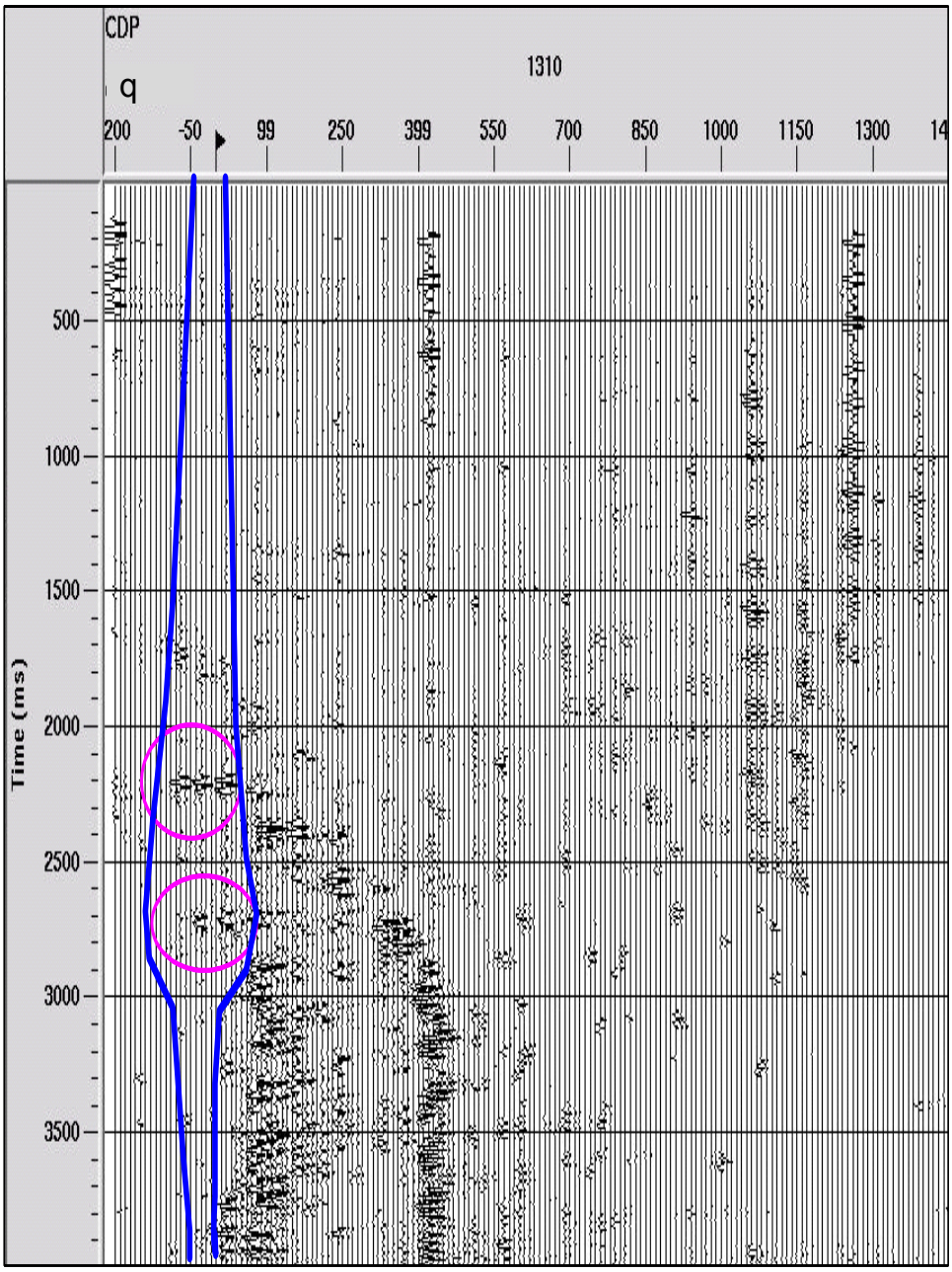

Figure 4.12 The Radon panel obtained by the optimized semblance-weighted Radon transform method. Primaries are indicated by circles. The blue curves indicate the muting boundaries.

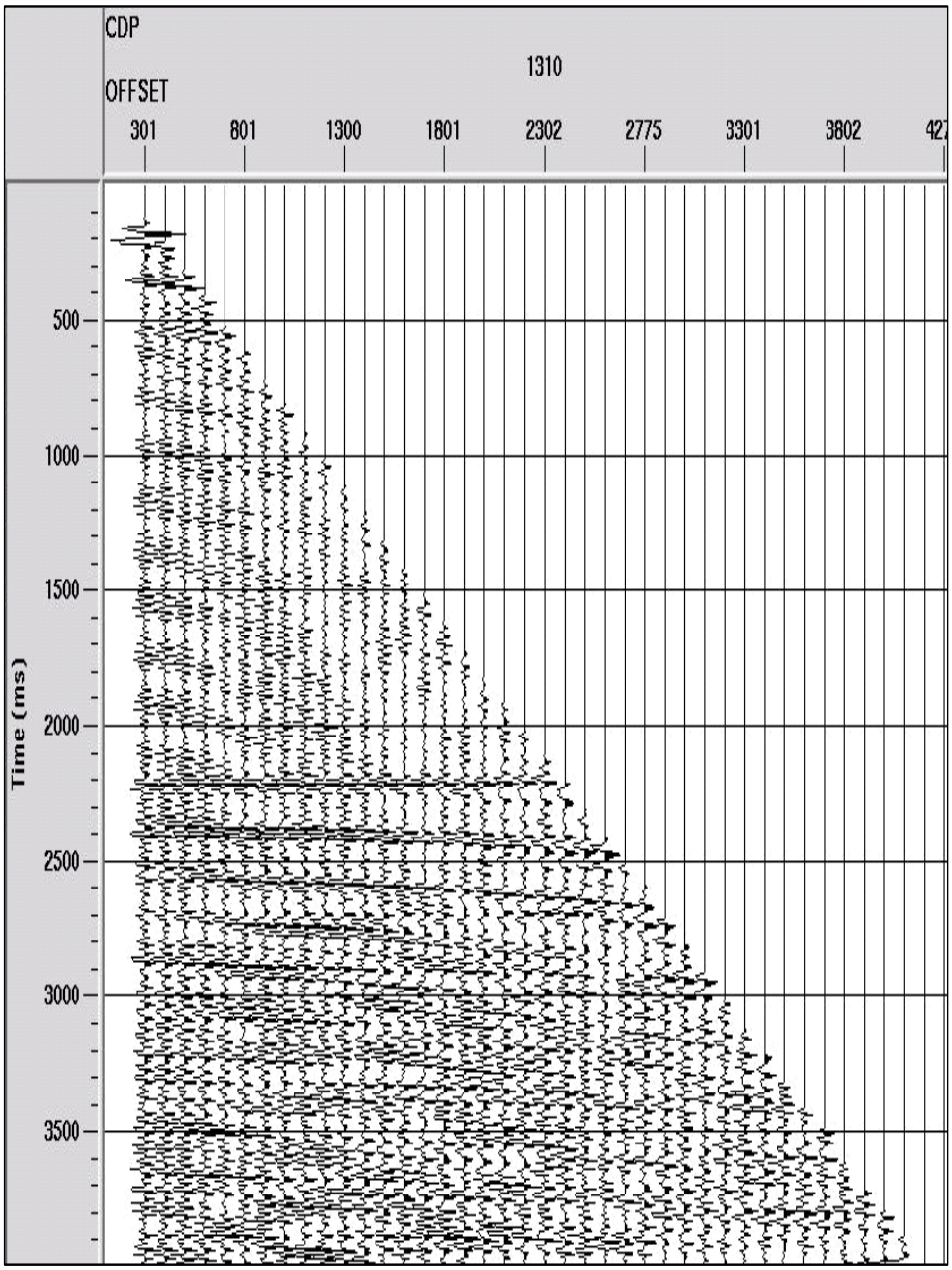

Figure 4.13 The full reconstruction of the CMP gather from Figure 4.12. (Scaled to Figure 4.9)

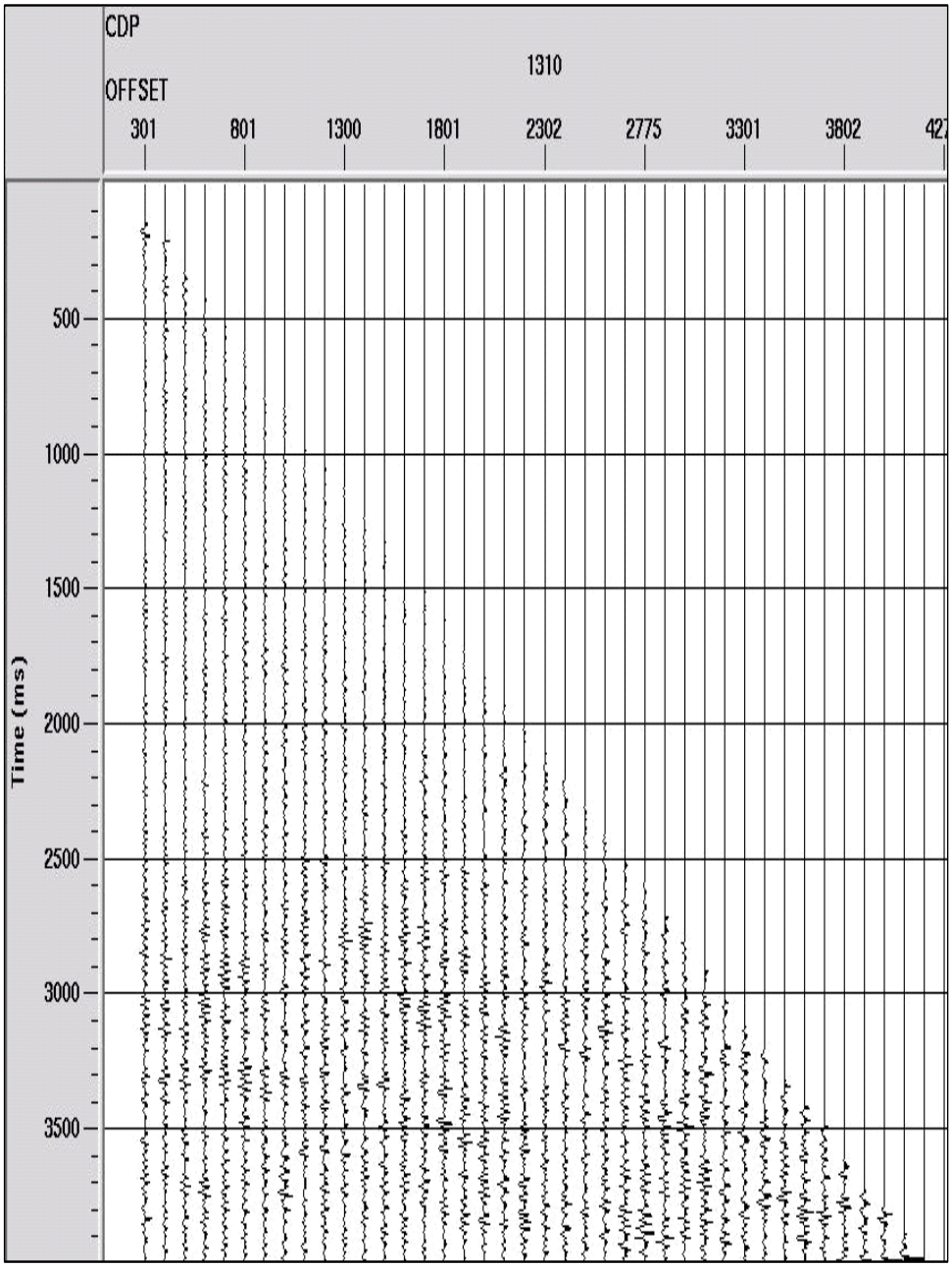

Figure 4.14 The difference between the full reconstruction and the original CMP gather.

(Scaled to Figure 4.9)

The two primaries located at around 0 ms on the q-axis, 2.2 s and 2.7 s in time, indicated by the pink circles, can easily be separated from the multiple reflections which are mainly on the positive side on the q-axis (Figure 4.12). The primaries are muted in this Radon panel, indicated by the blue curves in Figure 4.12, before the inverse Radon transform is performed so that only multiple reflections are reconstructed back to the time-space domain (Figure 4.15). The multiple-free gather is then obtained by subtracting the multiple-only gather from the original gather and the result is shown in Figure 4.16. We can see that the multiple-free gather is free of primaries and the primary-only gather contains only the primaries and random noise.

In order to further examine the processing results of the Radon transform, the modelled multiple gather and the primary gather are inverse NMO-corrected, as shown in Figure 4.17 and Figure 4.19, respectively and their semblance plots are shown in Figure 4.19 and Figure 4.20, respectively. Only energy from multiple reflections is left out in Figure 4.19 and only energy from primary reflections remains in Figure 4.20.

Although the Radon transform can have a hard time in short-period multiples, the example we used shows us that the Radon transform can be a great choice on multiple attenuation if the high-resolution algorithm is employed. For long-period multiples, the muting in the Radon domain is much easier and the Radon transform can do an even better job of multiple attenuation.

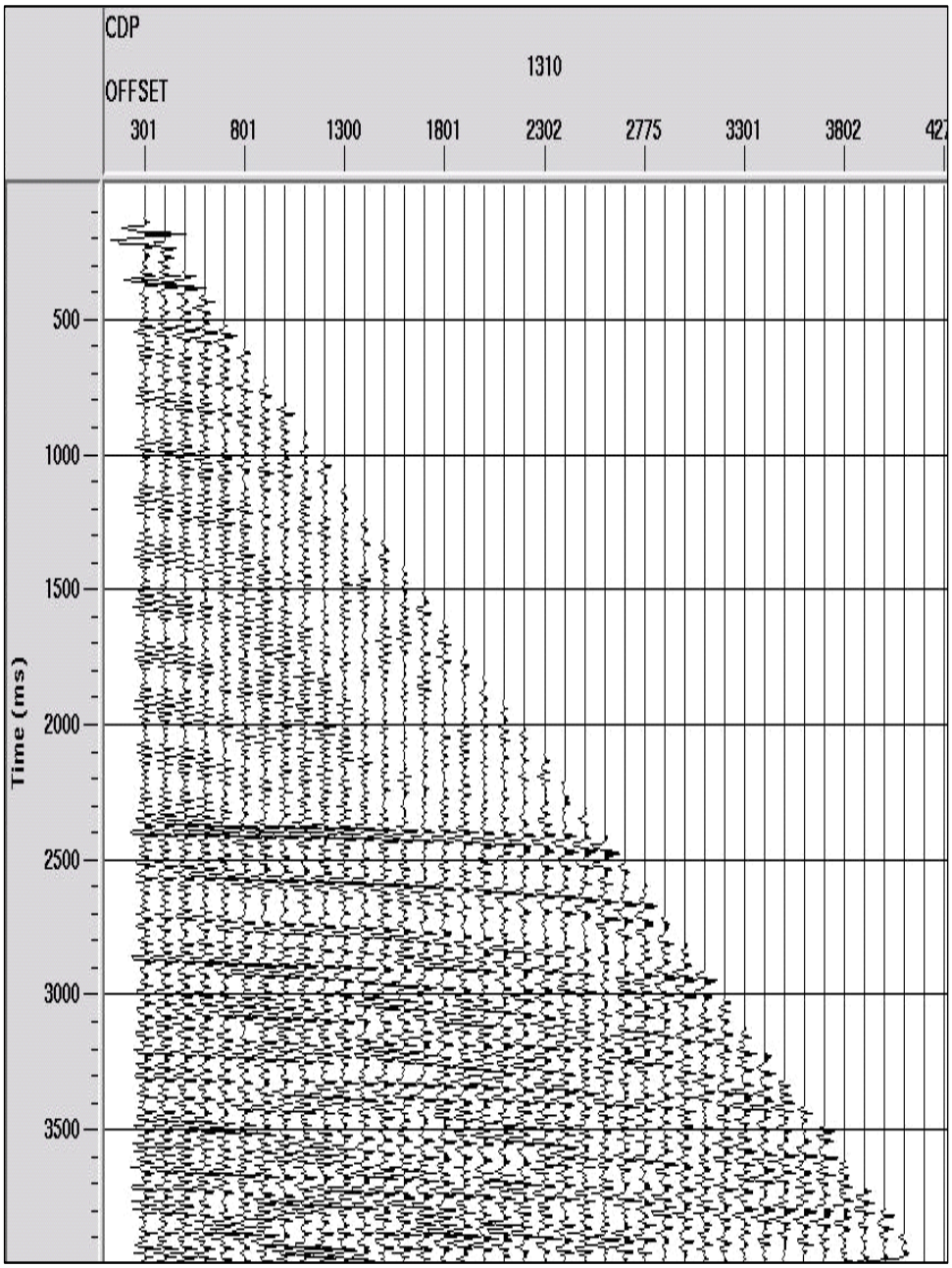

Figure 4.15 The reconstructed multiple-only gather. (Scaled to Figure 4.9)

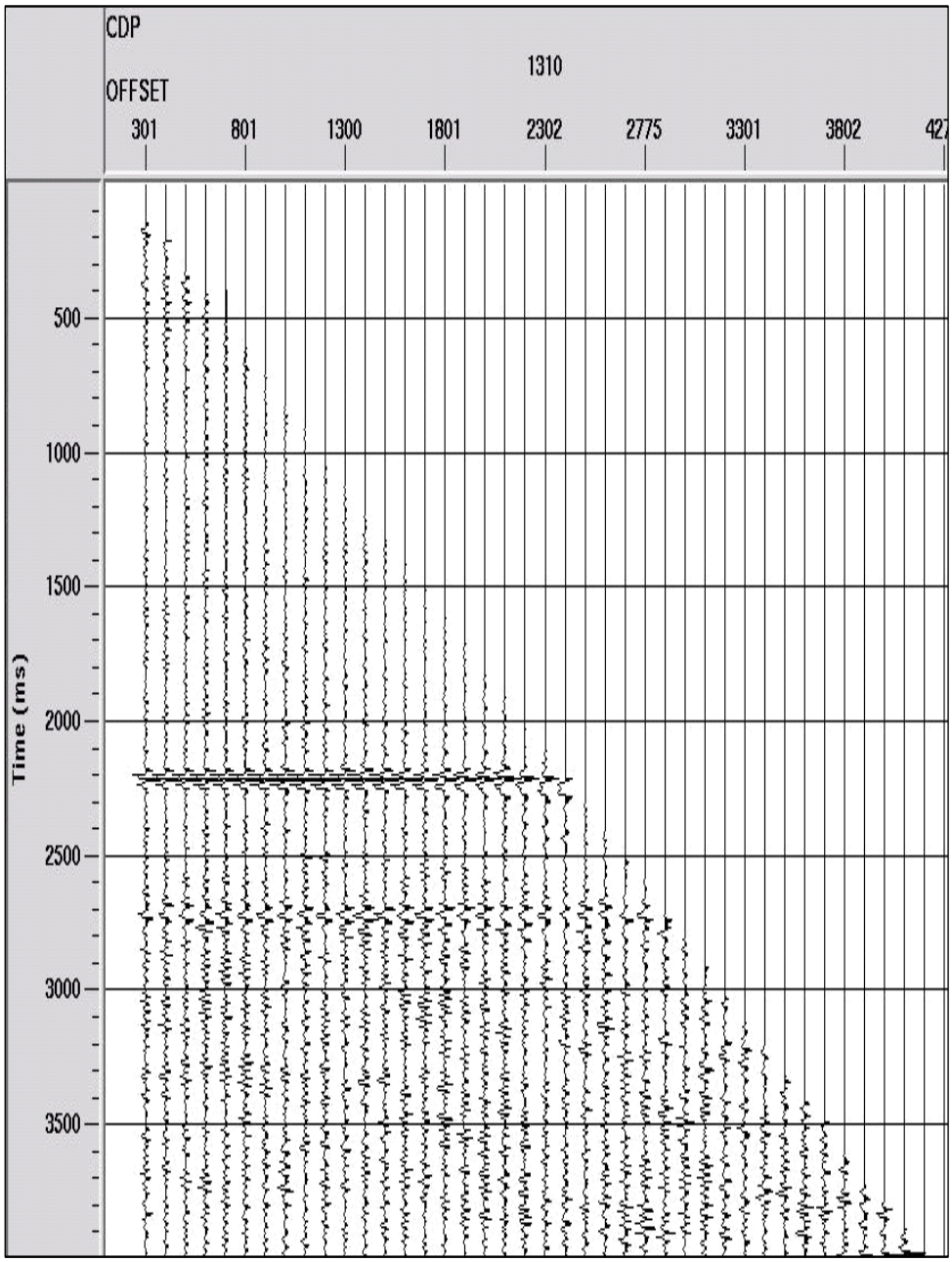

Figure 4.16 The modelled primary-only gather obtained by subtracting the multiple-only gather from the original CMP gather. (Scaled to Figure 4.9)

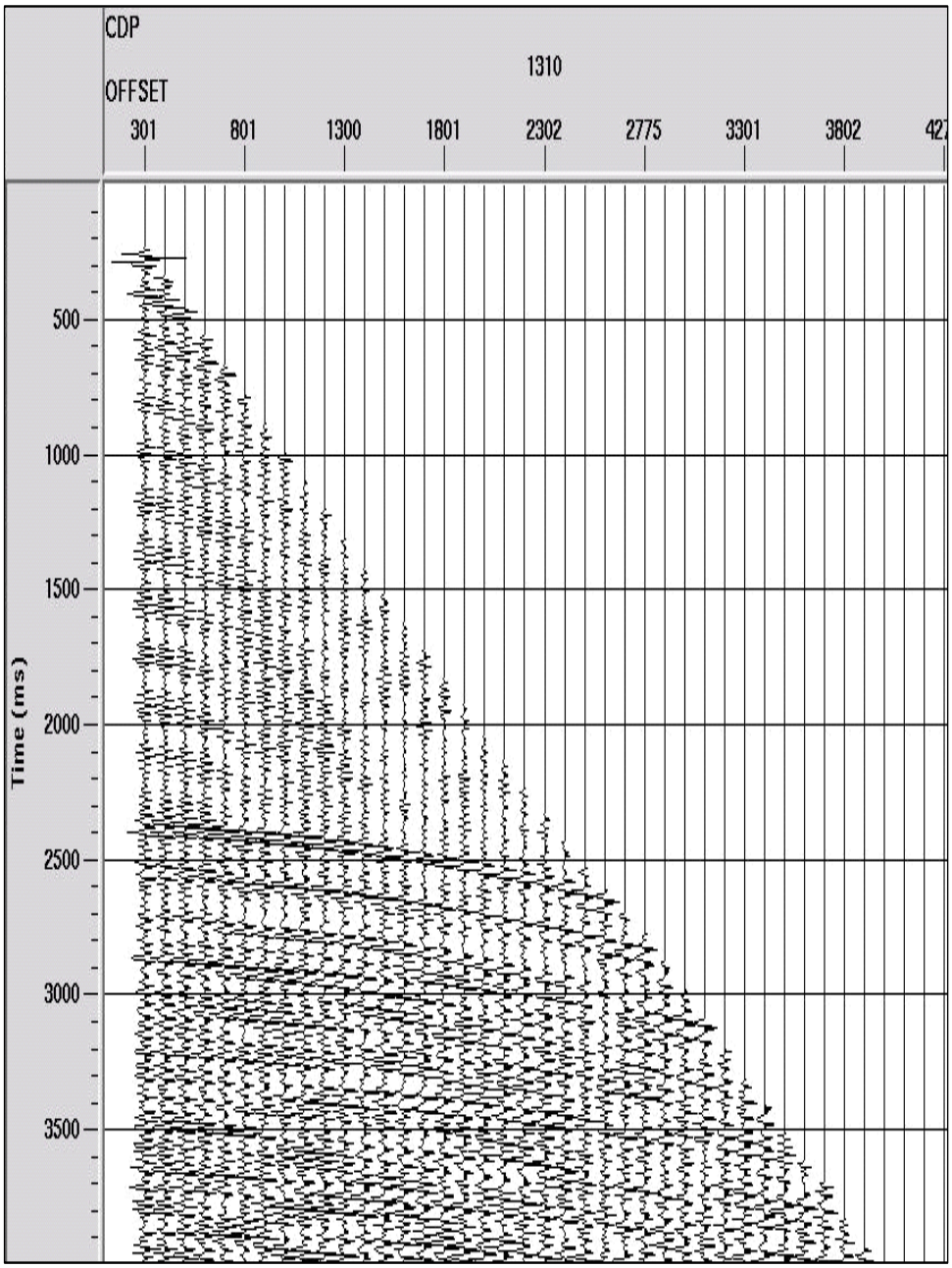

Figure 4.17 The inverse NMO-corrected multiple-only gather from Figure 4.15. (Scaled to Figure 4.9)

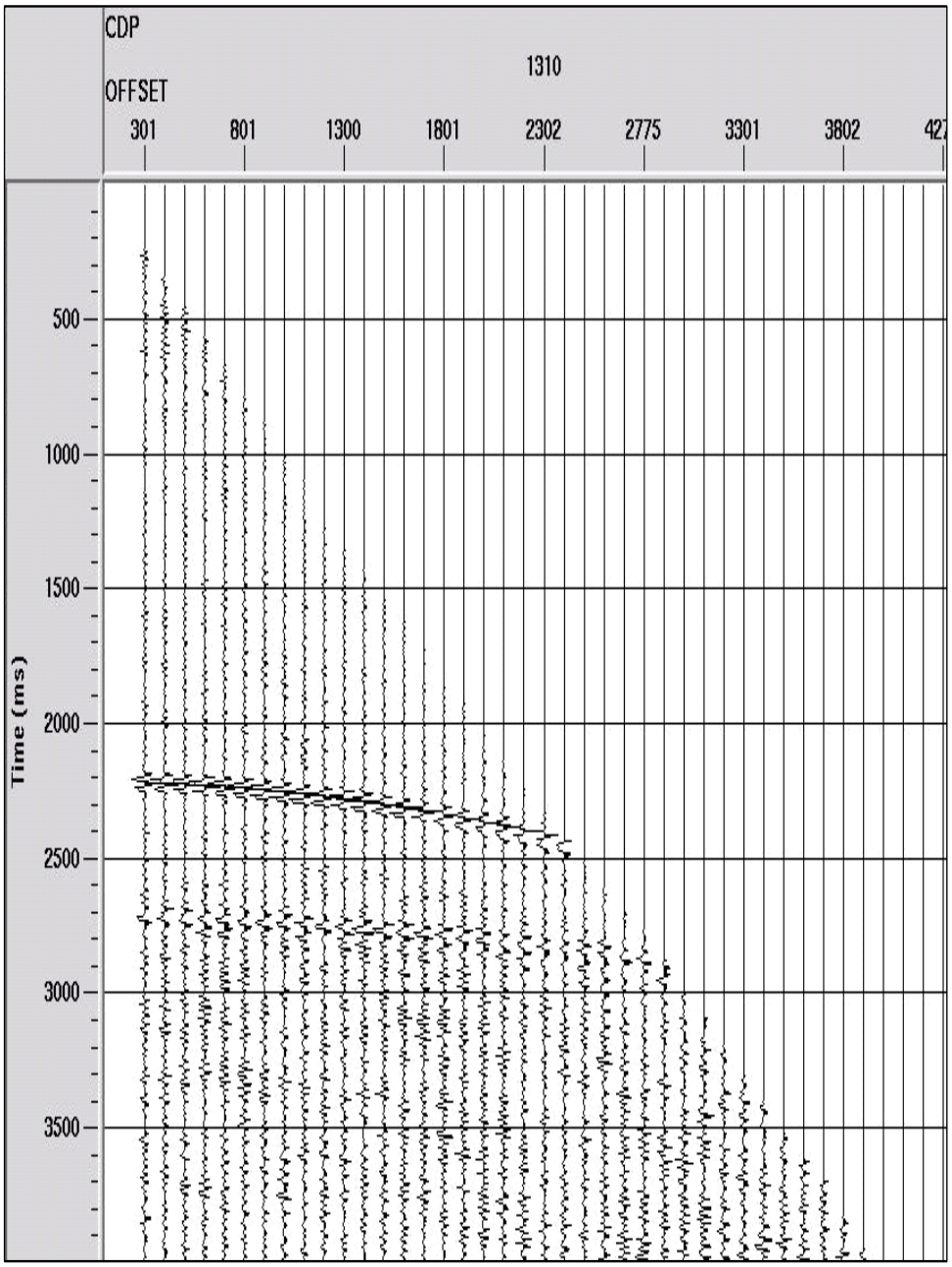

Figure 4.18 The inverse NMO-corrected primary-only gather from Figure 4.16. (Scaled to Figure 4.9)

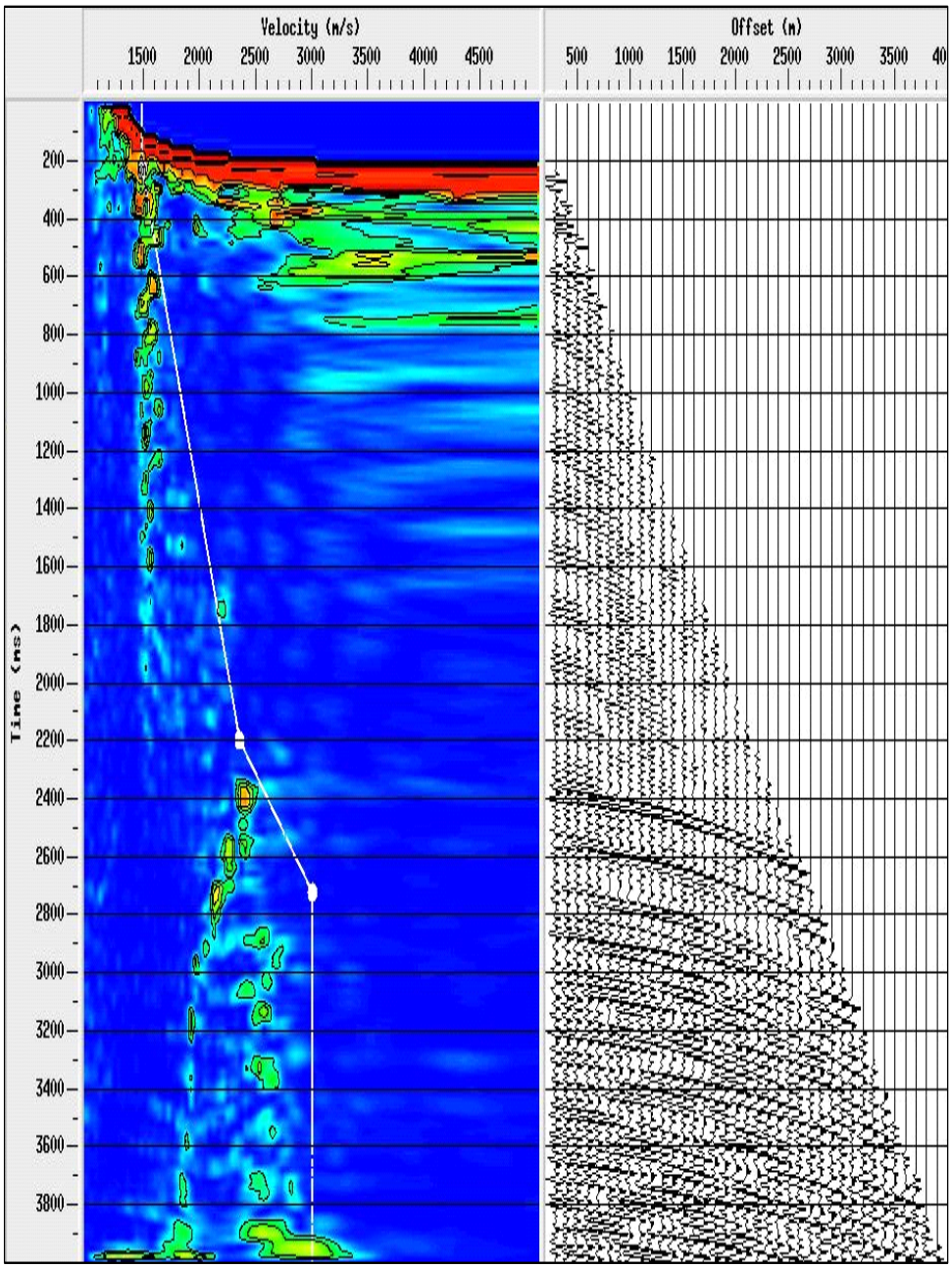

Figure 4.19 The semblance plot of the modelled multiple-only gather.

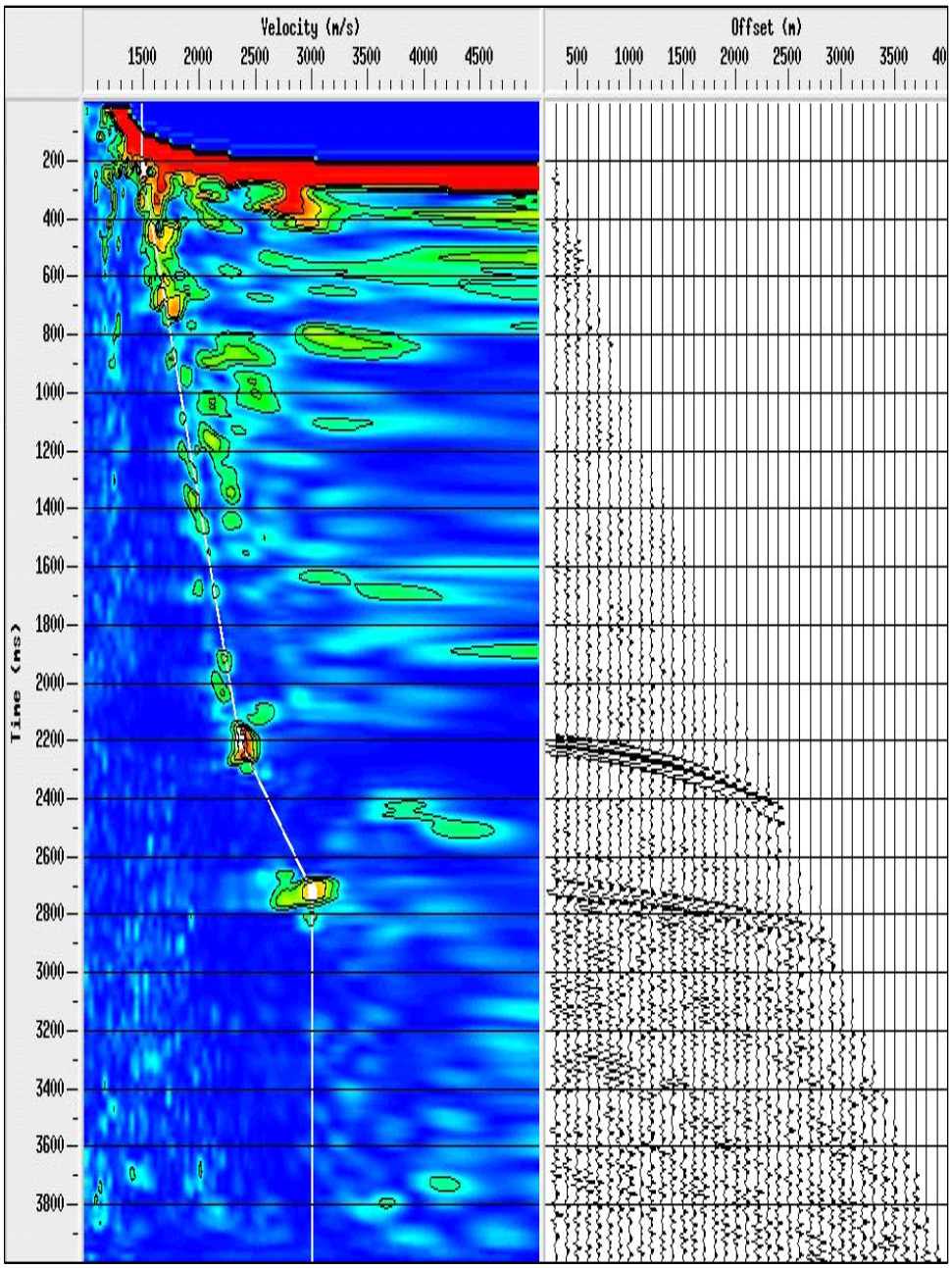

Figure 4.20 The semblance plot of the modelled primary-only gather.

The stack section without demultiple technique applied and the section with the optimized semblance-weighted Radon technique applied are shown in Figure 4.21 (a) and (b), respectively. Comparing the two sections, multiples are very strong in Figure 4.21 (a) and reduced dramatically in (b). Some weaker primary events become visible after multiple attenuation.

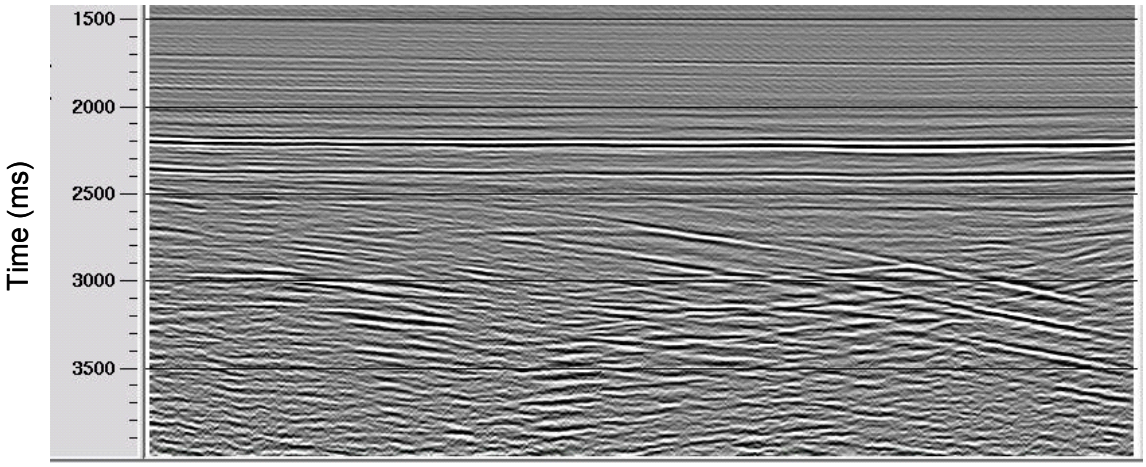

(a)

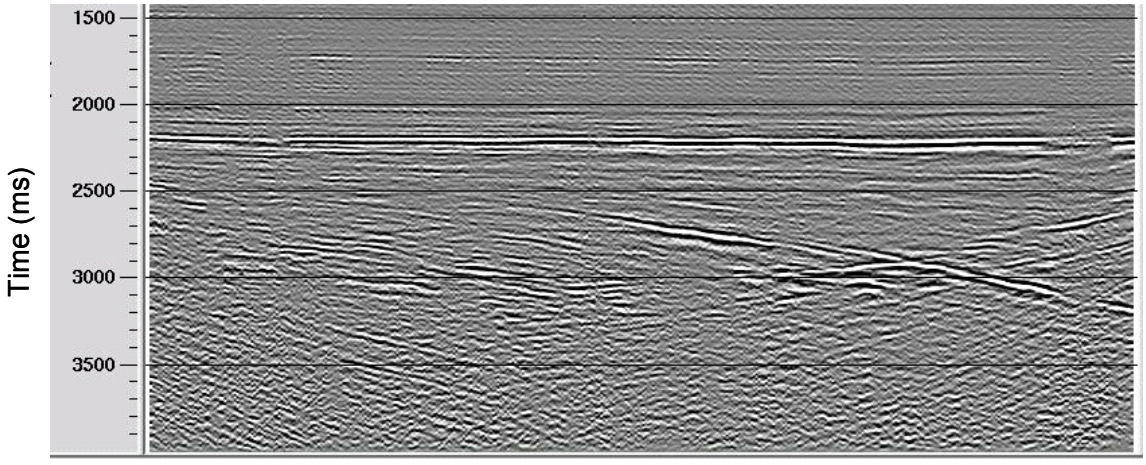

(b)

Figure 4.21 (a) The stack section without multiple attenuation technique applied; (b) the stack section with the optimized semblance-weighted Radon method applied on multiple attenuation.

Chapter Five: Conclusions

The problem of multiple reflections in exploration seismology is discussed in this thesis. In particular, various algorithms pertaining to the Radon transform have been analyzed. The parabolic Radon transform in the frequency domain has been an industry preference since its publication because of its time-invariant property and fast implementation in the frequency domain. But the hyperbolic Radon transform shows different characteristics from the parabolic Radon transform in that the former is time variant and it can't be implemented in the frequency domain so that its inversion becomes a difficult and very time consuming task.

An optimized semblance-weighting Radon method is analyzed and discussed in Chapter 3 and 4 with both synthetic and real datasets. This algorithm adopts the concept that the transform is implemented sequentially along the q-axis from strong to weak energy. Since there is no inversion involved in this algorithm, there isn't very much extra computational time expense in the hyperbolic Radon transform compared to the parabolic one if the optimized semblance-weighted Radon method is adopted. Therefore, this optimized method is superior to the frequency domain parabolic Radon transform because the seismic reflections including primaries and multiples exhibit hyperbolic characteristics in the time space domain. If long-offset data are involved, the parabolic Radon transform will induce significant resolution problems.

The application of this algorithm to the numerical and field data demonstrates the validity of the method. The optimized semblance-weighted Radon transform in time domain has many useful properties that will be of benefit to the seismic processing

industry such as velocity analysis. This method will be able to provide better resolution for velocity analysis compared to the current used semblance plot.

References

Alam, A., and Austin, J., 1981, Multiple suppression using slant stacks: Tech. Rep., Western Geophysical Company.

Backus, M.M., 1959, Water reverberations—their nature and elimination: Geophysics, 24, 233-261.

Bancroft, J. C., Geiger, H. D., and Margrave, G. F., 1998, The equivalent offset method of prestack time migration: Geophysics, 63, 2042-2053.

Bancroft, J. C., and Cao, Z., 2004, A comparison of CMP and EO gathers for multiple-attenuation: CSEG Abstract.

Beylkin, G., 1987, Discrete Radon transform: IEEE Trans. Acoust., Speech, and Signal Proc., ASSP-35, No.2, 162-172.

Bradshaw, A., and Ng, M., 1987, Multiple attenuation by parabolic stack Radon transform: Geo-X Systems internal paper.

Cary, P., 1998, The simplest discrete Radon transform: Presented at the 68th Ann. Internat. Mtg., Soc. Expl. Geophys., Expanded Abstracts, 1999-2002.

Castle, R. J., 1994, A theory of normal moveout: Geophysics, 20, 68-86.

Deans, S. R., 1983, The Radon transformation and some of its application: John Wiley and Sons, Inc.

Dix, C. H., 1955, Seismic velocities from surface measurements: Geophysics, 20, 68-86.

Durrani, T. S., and Bisset, D., 1984, The Radon transform and its properties: Geophysics, 49, 1180-1187.

Ellsworth, T. P., 1948, Multiple reflections: Geophysics, 13, 1-18.

Foster, D.J., and Mosher, C.C., 1992, Suppression of multiple reflections using the Radon transform: Geophysics, 57, 386-395.

Hampson, D., 1986, Inverse velocity stacking for multiple elimination: J. Can. Soc. Expl. Geophys., 22, 44-55.

Hemon, C. H., and Mace, D., 1978, Use of the Karhunen-Loeve transformation in seismic data processing: Geophysical Prospecting, 26, 600-626.

Hugonnet, P., and Canadas, G., 1995, Aliasing in the parabolic Radon transform: Presented at the 65th Ann. Internat. Mtg., Soc. Expl. Geophys., Expanded Abstracts, 1366-1369.

Jones, I. F., 1985, Application of the Karhunen-Loeve transformation in reflection seismic processing: Ph. D. Thesis, University of British Columbia.

Jones, I. F., and Levy, S., 1987, Signal-to-noise ratio enhancement in multichannel seismic data via the Karhunen-Loeve transform: Geophysical Prospecting, 35, 12-32.

Kelamis, P. G., Chiburis, E. F., and Shahryar, S., 1990, Radon multiple elimination, a practical methodology for land data: Presented at the 60th Ann. Internat. Mtg., Soc. Expl. Geophys., Expanded Abstracts, 1611-1613.

Kostov, C., 1990, Toeplitz structure in slant-stack inversion: Presented at the 60th Ann. Internat. Mtg., Soc. Expl. Geophys., Expanded Abstracts, 1618-1621.

Lines, L. R., and Treitel, S., 1984, Tutorial: A review of least-squares inversion and its application to geophysical problems. Geophysical Prospecting, 32, 159-186.

Malovichko, A. A., 1978, A new representation of the traveltime curve of reflected waves in horizontally layered media: Applied Geophysics, 91, 47-53, (in Russian).

Mayne, W. H., 1962, Common reflection point horizontal data stacking techniques: Geophysics, 27, 927-938.

Ng, M., and Perz, M., 2004, High resolution Radon transform in the *t-x* domain using "intelligent" prioritization of the Gauss-Seidel estimation sequence: Presented at the 74th Ann. Internat. Mtg, Soc. Expl. Geophys., Expanded Abstracts, 2160-2163.

Oppert, S. K., 2002, Radon methods for improved imaging of high-velocity layers using mode-converted energy: M.Sc. Thesis, Univ. of Calgary.

Oppert, S. K., and Brown, R. J., 2002, Improved Radon transforms for filtering of coherent noise, CREWES Research Report, 14.

Peacock, K. L., and Treitel, S., 1969, Predictive deconvolution—theory and practice: Geophysics, 34, 155-169.

Press, W. H., Flannery, B. P., Teukolsky, S. A., and Vetterling, W. T., 1986, Numerical recipes — The art of computing. Cambridge University Press.

Radon, J., 1917, Über die Bestimmung von Funktionen durch ihre Integralwerte Längs gewisser Mannigfaltigkeiten, Berichte Sächsische Akadamie der Wissenschaften, Leipzig, Math.-Phys. Kl., 69, 262-267.

Sacchi, M. D., and Ulrych, T. J., 1995, High-resolution velocity gathers and offset space reconstruction: Geophysics, 60, 1169-1177.

Sacchi, M. D., and Porsani, M., 1999, Fast high-resolution parabolic Radon transform: Presented at the 69th Ann. Mtg, Soc. Expl. Geophys., Expanded Abstracts, 1477-1480.

Schultz, P. S., and Claerbout, J. F., 1978, Velocity estimation and downward continuation by wavefront synthesis: Geophysics, 43, 691-714.

Stoffa, P. L., Buhl, P., Diebold, J. B., and Wenzel, F., 1981, Direct mapping of seismic data to the domain of intercept time and ray parameter — A plane-wave decomposition: Geophysics, 46, 255-267.

Taner, M. T., and Koehler, F., 1969, velocity spectra – digital computer derivation applications of velocity functions: Geophysics, 34, 859-881.

Taner, M. T., 1980, Long-period sea-floor multiples and their suppression: Geophys. Prosp., 28, 30-48.

Thorson, J. R., and Claerbout, J. F., 1985, Velocity-stack and slant-stack stochastic inversion: Geophysics, 50, 2727-2741.

Trad, D., 2001, Implementations and applications of the sparse Radon transform: Ph. D. Thesis, The University of British Columbia.

Trad, D., Ulrych, T. J., and Sacchi, M. D., 2002, Accurate interpolation with high-resolution time-variant Radon transforms: Geophysics, 67, 644-656.

Trad, D., Ulrych, T., and Sacchi, M. 2003, Latest views of the sparse Radon transform: Geophysics, 68, 386-399.

Treitel, S., Gutowski, P. R., and Wagner, D. E., 1982, Plane-wave decomposition of seismograms: Geophysics, 47, 1375-1401.

Turner, G., 1990, Aliasing in the tau-*p* transform and the removal of spatially aliased coherent noise: Geophysics, 55, 1496-1503.

Yilmaz, Ö., 1987, Seismic data processing: Soc. Expl. Geophys.

Yilmaz, Ö., 1989, Velocity-stack processing: Geophys. Prosp., 37, 357-382.

Yilmaz, Ö., and Taner, M. T., 1994, Discrete plane-wave decomposition by least-mean-square-error method: Geophysics, 59, 973-982.

Yilmaz, Ö., 2001, Seismic data analysis: Soc. Expl. Geophys.

Zhou, B., and Greenhalgh, S. A., 1994, Linear and parabolic τ-p transforms revisited: Geophysics, 59, 1133-1149.